POLITECNICO DI TORINO
Repository ISTITUZIONALE

Full-field deformation reconstruction of beams using the inverse Finite Element Method: Application to thin-walled structures

Original
Full-field deformation reconstruction of beams using the inverse Finite Element Method: Application to thin-walled structures / Roy, R., Surace, C., Gherlone, M.. - In: THIN-WALLED STRUCTURES. - ISSN 0263-8231. - ELETTRONICO. - 200:(2024), pp. 1-20. [10.1016/j.tws.2024.111907]

Availability:
This version is available at: 11583/2988319 since: 2024-05-13T12:12:45Z

Publisher:
Elsevier

Published
DOI:10.1016/j.tws.2024.111907

Terms of use:

This article is made available under terms and conditions as specified in the corresponding bibliographic description in the repository

Publisher copyright
Elsevier postprint/Author's Accepted Manuscript

© 2024. This manuscript version is made available under the CC-BY-NC-ND 4.0 license
http://creativecommons.org/licenses/by-nc-nd/4.0/.The final authenticated version is available online at:
http://dx.doi.org/10.1016/j.tws.2024.111907

(Article begins on next page)

12 November 2026

Full-Field Deformation Reconstruction of Beams using the inverse Finite Element Method: Application to Thin-Walled Structures

Rinto Roy[1,*], Cecilia Surace[2] and Marco Gherlone[1]

[1]Department of Mechanical & Aerospace Engineering,

Politecnico di Torino, Corso Duca degli Abruzzi, 24, 10129 Torino, Italy

[2]Department of Structural, Geotechnical & Building Engineering,

Politecnico di Torino, Corso Duca degli Abruzzi, 24, 10129 Torino, Italy

[*]Corresponding Author: rinto.roy@polito.it

Abstract:

This work presents a methodology for the real-time structural deformation reconstruction of solid or thin-walled prismatic beams using discrete strains. Based on the 1D inverse Finite Element Method (iFEM), the approach combines the beam kinematics of Timoshenko theory, strain-displacement relations, and the finite element discretisation framework to reconstruct the full-field deformations of beams with any general cross-section. Although applicable for any general class of beams, the present work investigates its experimental application specifically to conventionally and additively manufactured thin-walled beams discretised using various low- and high-order inverse beam elements. The results demonstrate the method's accuracy and robustness, albeit influenced by the element discretisation scheme and the number of strain sensors used.

Keywords: Inverse Problem, Shape Sensing, Thin-walled Beam, Additive Manufacturing, Timoshenko beam, Fibre Optic Sensors

1 Introduction

Aircraft structures are designed to operate reliably over a wide spectrum of structural loads generated due to aircraft manoeuvrers in different operational conditions or environments. Furthermore, any technically feasible design has to be weighed against its economic feasibility, with structural mass being the key impediment. Contemporary designs have achieved a suitable compromise between strength and mass by adopting thin-walled structural members to provide high strength and reliability without significantly contributing to the structural mass. With the emergence and implementation of aircraft Structural Health Monitoring (SHM) systems in recent decades, additional improvements to aircraft safety and operational costs can also be expected. [1]. However, such an SHM system should ideally be able to monitor the mechanical behaviour and evaluate the integrity of the various solid or thin-walled members that make up the airframe. Implicit in the above challenge is the inverse problem of sensing or monitoring structural displacements (i.e., shape change) in real-time. This problem can be solved using *shape-sensing* methods that allow structural displacements to be reconstructed from embedded strain-sensor measurements.

Shape-sensing methods are also relevant in addressing another key limitation of contemporary airframe designs, i.e., their relatively high structural rigidity that limits their operational envelope. In contrast, flight solutions produced by biological systems are more compliant and deformable (e.g., insect and bird wings), with the ability to perform a wider range of missions or manoeuvrers [2, 3]. Morphing airframe designs can yield greater efficiency and multi-mission adaptivity. In this context, shape-sensing methods can be used to develop control strategies that efficiently integrate morphing actuation and sensing elements to provide greater performance.

Numerous shape-sensing approaches have been developed in literature [4], with the main ones briefly recounted here. Structural deformations can be obtained by integrating experimental strain measurements under the framework of classical beam theories [5, 6]. However, this approach is limited in terms of the possible geometries analysed, while accuracy heavily depends on the number of strain measurements. Alternatively, the displacement field can be modelled as a weighted superposition of basis functions (including vibration mode shapes), where the corresponding weights are subsequently evaluated using experimental strain measurements [7, 8]. The optimal choice of basis functions combined with the need for a system model or experimental data proves to be a limitation in this case. Mapping sensor measurements to deformations using Neural Networks can also serve as a purely data-driven solution to the problem [9], with its associated limitations in terms of data availability and efficient network training.

Shape sensing based on a least-squares variational principle has gained significant attention recently, with the inverse Finite Element Method (iFEM) [10, 11] the pioneering work on this topic. As iFEM is based on the strain-displacement relations, no information regarding material properties or operational conditions (or system model) is required. At the same time, the use of a finite element discretisation framework ensures complex geometries can be analysed. Additionally, its ability to produce accurate and robust results using a sparse set of strain measurements makes it an attractive alternative to other shape-sensing techniques. Initial iFEM efforts focused on plate and shell structures [11], with the development of the three-node constant strain shell element, iMIN3, by Tessler et al. [12]. The element is based on Mindlin theory and uses C^0-continuous anisoparametric shape functions leading to an improved treatment of transverse shear in the thin plate regime. Subsequently, higher-order elements such as the four-node quadrilateral shell element iQS4 [13], the eight-node curved shell element iCS8 [14], and the three-node shell element i3-RZT for multi-layered composite structures [15] were developed. These fundamental developments have been accompanied by the adoption of iFEM for various

applications, primarily in the domain of SHM. Notable works include an iFEM-based damage detection approach for plates using strain mode differences that adopted deep neural network to localize and quantify the damage [16], coupling iFEM and peridynamics theory for damage prognosis in plates by reconstructing structural deformations internal to the damaged zone [17], and iFEM-based delamination [18], debond [19], and impact damage [20] detection strategies for composite plate and stiffened panel structures.

The work of Gherlone et al. [21] laid the theoretical foundation of the one-dimensional (1D) iFEM for beam and frame structures. The 1D iFEM discretises the structure using inverse beam elements (developed based on Timoshenko theory [22]) and attempts to match a set of analytical and experimental sectional strains in a least-squares sense. These sectional strains represent the axial, bending, transverse shear, and torsional deformation of a beam section. Initial validation of these inverse beam elements was performed on a cantilevered beam with a simple circular profile under static and dynamic loading conditions [21, 23].

Later developments include beam elements based on Euler-Bernoulli theory for modelling slender beams [24] and coupling with Refined Zigzag Theory (RZT) for analysing composite beams [25]. Efforts to analyse greater geometrical and material complexities in beams include the development of curved beam elements [26], analysing material non-linearities [27], and the use of isogeometric analysis to model variable section beams [28, 29], and complex loading scenarios [30]. Further enhancements were also proposed by You et al. [31] to ensure robust non-singular solutions. Other relevant works include using optimization techniques to identify optimal sensor locations for efficient shape sensing [32, 33, 34] and an application for real-time monitoring of a radio telescope reflector [35]. Despite the abundance of numerical and experimental results, various gaps still need to be addressed. Existing works have mainly prioritised beam bending deformation reconstruction, with less emphasis on torsion. The need for new formulations to handle more geometrically complex beam structures is

also evident. Roy et al. [36, 37] proposed a solution to these problems by extending the original 1D iFEM formulation to analyse prismatic beams with any arbitrary profile. A key achievement of this work is the accurate prediction of both bending and torsional deformations, which was demonstrated numerically for various cantilevered prismatic airfoil beams [37, 38].

This work builds on previous efforts by providing an experimental validation for the 1D iFEM methodology, specifically for the shape sensing of thin-walled prismatic beams with complex cross-sections. As most prior investigations involved numerical data or simple beam geometries, the results presented in this work provide a further layer of technical readiness for the methodology. These experimental investigations also include a novel application of the 1D iFEM, specifically for monitoring additively manufactured beam structures. Additionally, a novel iFEM formulation for thin-walled beams undergoing coupled bending, torsion, and warping deformation is also introduced, and the inverse elements developed based on it are validated using the experimental shape sensing examples. Aggregating all the various low and high-order inverse beam elements proposed in the literature and developed by the authors, this work provides an exhaustive comparison of performance between the elements in terms of the accuracy of the transverse deflection or torsional rotation reconstruction, computational efficiency, and the number of sensors required in each case. Such a comparative characterisation of element performance provides a useful framework for element selection or choosing the fidelity of discretisation required for future problems involving arbitrary geometries, loading conditions, or sensor configurations.

The paper is organised as follows: Section 2 provides a brief theoretical discussion of the 1D iFEM formulation and introduces the inverse elements used in this work. The methodology is applied experimentally for the shape sensing of a thin-walled C beam in Section 3 and, subsequently, to an additively manufactured airfoil beam in Section 4. In both sections, the beams are discretised using various inverse beam elements, and their respective results are compared

and contrasted. Finally, Section 5 concludes with the main achievements and areas for future work.

2 Inverse Finite Element Method for Beams

This section briefly discusses the 1D iFEM formulation for beams and frames. The underlying theory was initially proposed by Gherlone et al. [21] and later expanded by Roy et al. [37] for predicting the transverse shear and torsional deformation of prismatic beams with any general profile. The 1D iFEM framework for prismatic beams, and the inverse beam elements so derived from it, are discussed in this section. Interested readers are encouraged to refer to Ref. [21, 37] for additional discussions.

2.1 Least-Squares Error Functional

Displacement reconstruction using the 1D iFEM is based on matching a vector of analytical, $\mathbf{e}(\mathbf{u})$, and experimental, $\mathbf{e}^{\epsilon}$, sectional strains in a least-squares sense [21] using an error functional defined as

$$\Phi(\mathbf{u}) = \|\mathbf{e}(\mathbf{u}) - \mathbf{e}^{\epsilon}\|^2 \tag{1}$$

where $\mathbf{u}$ is the vector of kinematic variables used to describe the beam kinematics and the superscript $(*)^{\epsilon}$ represents an experimentally computed quantity. The iFEM methodology is based on a variational formulation where the structural domain is discretised using finite elements. The error functional for each element, Φ^e, can be written as

$$\Phi^e = \mathbf{w} \cdot \mathbf{\Phi}^s = \sum_{k=1}^{6} w_k^e \Phi_k^e \tag{2}$$

where $\mathbf{w}$ is a vector of weighing coefficients for controlling the enforcement of the least-squares compatibility, and $\mathbf{\Phi}^s$ is a vector of error functionals, Φ_k^e. The value of weights associated with each functional also ensures the dimensional

consistency of Eq. 2. Each functional Φ_k^e corresponds to the k^{th} sectional strain, e_k, and is defined as

$$\Phi_k^e = \frac{l_e}{N} \sum_{i=1}^{N} \left[e_k(x_i) - (e_k^\epsilon)_i \right]^2 \quad , \quad (k = 1, ..., 6) \tag{3}$$

where l_e is the element length and N is the number of axial beam sections, x_i, instrumented with strain sensors. The analytical sectional strains are computed from the kinematic field of the structure, $\mathbf{u}(x)$, which in turn is obtained by interpolating the nodal degrees-of-freedom (DOF) using element shape functions

$$\mathbf{u}(x) = \mathbf{N}(x)\mathbf{u}^e \tag{4}$$

where $\mathbf{N}(x)$ is the matrix of shape functions and $\mathbf{u}^e$ is a vector of nodal DOF. Assuming the beam obeys the small-strain hypothesis, the analytical sectional strains are derived from Eq. 4 using the linear strain-displacement relations

$$\mathbf{e}(\mathbf{u}) = \mathbf{B}(x)\mathbf{u}^e \tag{5}$$

where $\mathbf{B}(x)$ is the matrix of shape function derivatives.

The element error functional is solved by substituting Eq. 5 in Eq. 2 and minimizing the functional with respect to the nodal DOF to obtain a series of linear algebraic equations

$$\mathbf{k}^e \mathbf{u}^e = \mathbf{f}^e \tag{6}$$

The matrix $\mathbf{k}^e$ and vector $\mathbf{f}^e$ are the weighted sum of contributions from each sectional strain

$$\mathbf{k}^e = \sum_{k=1}^{6} w_k^e \mathbf{k}_k^e \quad , \quad \mathbf{f}^e = \sum_{k=1}^{6} w_k^e \mathbf{f}_k^e \tag{7}$$

where each sectional strain contribution is defined in terms of the shape function derivatives

$$\mathbf{k}_k^e = \frac{l_e}{N} \sum_{i=1}^{N} \left[\mathbf{B}_k^T(x_i) \mathbf{B}_k(x_i) \right] \quad , \quad \mathbf{f}_k^e = \frac{l_e}{N} \sum_{i=1}^{N} \left[\mathbf{B}_k^T(x_i) (e_k^\epsilon)_i \right] \tag{8}$$

The system matrix $\mathbf{k}^e$ is only a function of strain sensor positions within the element, whereas the vector $\mathbf{f}^e$ is a function of the sensor positions and the experimental strain measurements. The necessary local coordinate transformations are applied, and all element contributions are assembled to obtain the global set of equations for the beam

$$\mathbf{KU} = \mathbf{F} \tag{9}$$

The boundary conditions are imperative to solve Eq 9. Similar to the direct FEM, boundary conditions are applied by constraining the relevant nodal DOF against the rigid-body motion and ensures the system matrix, $\mathbf{K}$, is non-singular. Subsequently, $\mathbf{K}$ can be inverted, and Eq 9 solved to obtain the iFEM reconstructed nodal displacements $\mathbf{U}$. As $\mathbf{K}$ is only a function of the sensor positions, once inverted, it does not need to be recomputed. Hence, for every update in the strains (i.e., of $\mathbf{F}$), the displacements can be evaluated very computationally efficiently, making it ideal for real-time monitoring applications with minimal latency.

The analytical sectional strains, $\mathbf{e}(\mathbf{u})$, are a function of the kinematic field of the beam, whereas $\mathbf{e}^\epsilon$ is computed using experimental strain measurements from sensors attached or embedded on the beam structure. The computation of these quantities is discussed further in the following sections.

2.2 Inverse Beam Element Formulation

Let us consider a general prismatic beam (as shown in Fig. 1) defined in the three-dimensional (3D) Cartesian coordinates, $\mathbf{x} \equiv (x, y, z)$. The beam has a length L and is made of a homogeneous isotropic material with Young's modulus E, shear modulus G, and Poisson's ratio ν. The coordinate system origin is located at the root of the beam, with the $x-$axis parallel to the beam axis and passing through the shear centre of the cross-section, and y and z forming the two transverse axes. The properties of the section profile are: cross-sectional

area A, second area moments I_{yy} and I_{zz}, and torsional constant I_t.

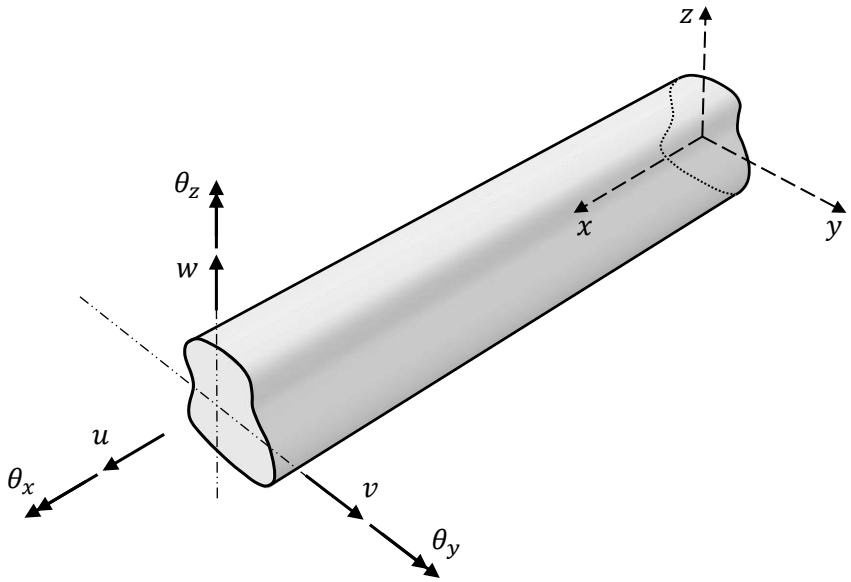

Figure 1: The reference coordinate system and kinematic variables used to describe the beam deformations

2.2.1 Analytical Sectional Strains

Let us assume the beam or frame structure to be subjected to any general loading condition composed of concentrated, distributed or pressure loads. The action of these loads generates axial stretching, bending, transverse shear and torsional deformation of the beam. These beam deformations can be modelled using an inverse element formulated based on the kinematic assumptions of Timoshenko beam theory [22, 23], where the Cartesian components of the displacement vector can be defined in terms of the kinematic variables $\mathbf{u} \equiv \{u, v, w, \theta_x, \theta_y, \theta_z\}^T$ as

$$\begin{aligned} u_x(x,y,z) &= u(x) + z\theta_y(x) - y\theta_z(x) \\ u_y(x,y,z) &= v(x) - z\theta_x(x) \\ u_z(x,y,z) &= w(x) + y\theta_x(x) \end{aligned} \tag{10}$$

where u_x, u_y, and u_z are the displacements computed at any beam point along the x, y and z-axis, respectively. The kinematic variables, u, v and w, are the beam displacements at the shear centre, while θ_x, θ_y and θ_z are the torsional and bending rotations about the x, y and z-axis, respectively (kinematic variables are defined in Fig. 1).

For small beam displacements, the axial and transverse shear strains can be obtained from Eq. 10 using the linear strain-displacement relations

$$\begin{aligned} \varepsilon_x(x,y,z) &= u_{x,x} = e_1(x) + ze_2(x) + ye_3(x) \\ \gamma_{xz}(x,y,z) &= u_{x,z} + u_{z,x} = e_4(x) + ye_6(x) \\ \gamma_{xy}(x,y,z) &= u_{x,y} + u_{y,x} = e_5(x) - ze_6(x) \end{aligned} \tag{11}$$

where e_i, $(i = 1, ..., 6)$ are the six sectional strains describing beam deformation. They are defined along the beam axis and correspond to the axial stretching, bending curvatures, transverse shear, and rate of twist of the beam, respectively, and are written in vector form as

$$\begin{aligned} \mathbf{e(u)} &= \{e_1, e_2, e_3, e_4, e_5, e_6\}^T \\ &= \{u_{,x}, \theta_{y,x}, -\theta_{z,x}, w_{,x} + \theta_y, v_{,x} - \theta_z, \theta_{x,x}\}^T \end{aligned} \tag{12}$$

The weighing coefficient vector of Eq. 2 is defined using the geometrical properties of the beam cross-section,

$$\mathbf{w} = \{w_1^0, w_2^0(I_{yy}/A), w_3^0(I_{zz}/A), w_4^0, w_5^0, w_6^0(I_t/A)\} \tag{13}$$

The weighting coefficients of Eq. 13 serve a two-fold purpose. First, they ensure the dimensional consistency of the error functional (Eq. 2). Second, they aid in formulating inverse elements that have no experimentally measured strains. In such cases, the contribution of the corresponding element error functional is penalized by setting the weights to a small value ($w^0 = 10^{-4}$). For elements with strain data, the weighting coefficients are set to unity ($w^0 = 1$).

Eq. 12 defines the analytical sectional strains of the beam initially introduced in Eq. 1. The calculation of its experimental counterparts is discussed in the next section.

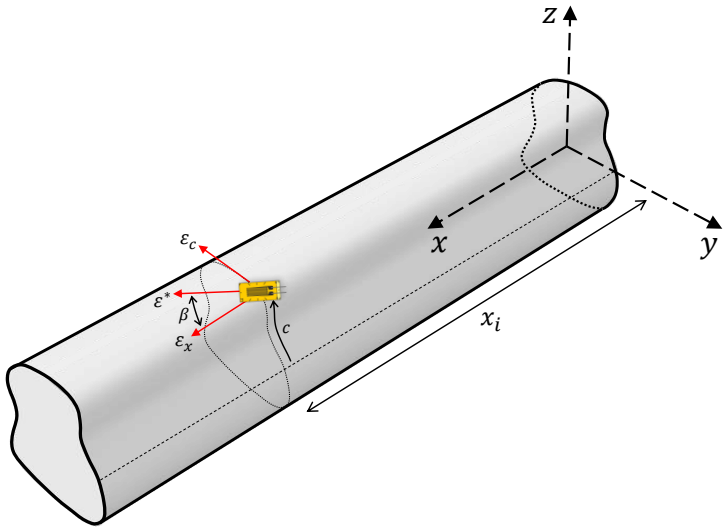

Figure 2: Definition of the location, orientation, and strain components measured by a strain gauge mounted on the beam surface

2.2.2 Experimental Sectional Strains

The six sectional strains, $\mathbf{e}^{\epsilon} \equiv \{e_1^{\epsilon}, e_2^{\epsilon}, e_3^{\epsilon}, e_4^{\epsilon}, e_5^{\epsilon}, e_6^{\epsilon}\}^T$, are computed using experimental strain measurements from sensors instrumented on the beam surface. Among these, the latter three correspond to the transverse shear and torsional deformation of the beam, respectively, and are a function of the beam profile. To relate the transverse shear strain distribution over the cross-section of any beam profile to e_j^{ϵ} $(j = 4-6)$, which are defined based on 1D beam theories, certain shear coefficients, $k_{\epsilon y}$ and $k_{\epsilon z}$, and functions, f_1, f_2, and f_3, are introduced [37]. These coefficients relate the maximum shear strain on the beam surface to the equivalent transverse shear strain at the shear centre, while the functions capture the surface shear strain distribution under transverse and torsional loads. These quantities are only a function of the beam profile and can

be computed using exact analytical solutions based on the theory of elasticity, or numerically using results from a high-fidelity FEM model of the beam. For a non-prismatic beam, they are a function of $x-$coordinate as they vary based on the beam profile at each axial section.

The beam is assumed to be instrumented with a set of strain sensors, either strain gauges or fibre optics. The measured strains are located at N discrete axial locations x_i $(i = 1, ..., N)$, and oriented at an angle β with respect to the x-axis (see Fig. 2). The surface strain measurement ε^* can be written in terms of the experimental sectional strains e_j^ϵ $(j = 1 - 6)$ as [37]

$$\begin{aligned}\varepsilon^*(x_i, c, \beta) = (e_1^\epsilon(x_i) + e_2^\epsilon(x_i)z(c) + e_3^\epsilon(x_i)y(c))\,(\cos^2\beta - \nu\sin^2\beta) + \\ \left(\frac{1}{k_{\epsilon z}}e_4^\epsilon(x_i)f_1(c) + \frac{1}{k_{\epsilon y}}e_5^\epsilon(x_i)f_2(c) + e_6^\epsilon(x_i)f_3(c)\right)\cos\beta\sin\beta\end{aligned} \tag{14}$$

where c is the local circumferential coordinate of the beam section in the counter-clockwise direction (see Fig. 2). The solution of Eq. 14 requires at least six experimental strain measurements per axial section x_i. For a detailed derivation of Eq. 14 and the computation of shear functions and coefficients, refer to Ref. [37].

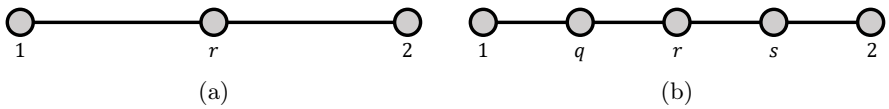

(a) (b)

Figure 3: Nodal topology for (a) iTM2D0 and (b) iTM2D1

2.2.3 Element Interpolations

The element interpolations previously developed by Gherlone et al. [21] are also used for this work and correspond to beam deformations under two separate load cases. The first models a beam under a general concentrated tip load where e_1, e_4, e_5, and e_6 are a constant, and the bending curvatures, e_2 and e_3, vary linearly across the element. The interpolation of kinematic variables within the

element in terms of the natural coordinates, $\eta \in [-1, 1]$, is given as [21]

$$\begin{aligned} u(\eta) &= \sum_{i=1,2} L_i^{(1)}(\eta) u_i \qquad\qquad , \quad \theta_x(\eta) = \sum_{i=1,2} L_i^{(1)}(\eta)\theta_{xi} \\ v(\eta) &= \sum_{i=1,2} L_i^{(1)}(\eta) v_i - \sum_{j=1,r,2} N_j^{(3)}(\eta)\theta_{zj} \quad , \quad \theta_y(\eta) = \sum_{i=1,r,2} L_i^{(2)}(\eta)\theta_{yi} \\ w(\eta) &= \sum_{i=1,2} L_i^{(1)}(\eta) w_i + \sum_{j=1,r,2} N_j^{(3)}(\eta)\theta_{yj} \quad , \quad \theta_z(\eta) = \sum_{i=1,r,2} L_i^{(2)}(\eta)\theta_{zi} \end{aligned} \tag{15}$$

where $L_i^{(1)}$ and $L_i^{(2)}$ are Lagrange polynomials, and $N_j^{(3)}$ are cubic functions. The beam element so developed (named 0^{th}-order element in Ref. [21]) is referred to as 'iTM2D0' in this work (see Fig. 3a). For an accurate numerical integration of Eq. 1, each iTM2D0 requires sectional strains from at least two axial sections, leading to a total of at least 12 strain measurements.

The second case models a beam subjected to uniform transverse distributed loads where e_1 and e_6 are a constant, e_4 and e_5 vary linearly, and e_2 and e_3 have a parabolic variation across the element. The interpolation of kinematic variables is given as [21],

$$\begin{aligned} u(\eta) &= \sum_{i=1,2} L_i^{(1)}(\eta) u_i \qquad , \quad \theta_x(\eta) = \sum_{i=1,2} L_i^{(1)}(\eta)\theta_{xi} \\ v(\eta) &= \sum_{i=1,q,r,s,2} L_i^{(4)}(\eta) v_i \quad , \quad \theta_y(\eta) = \sum_{i=1,2} L_i^{(1)}(\eta)\theta_{yi} + \sum_{j=1,q,r,s,2} M_j^{(3)}(\eta) w_j \\ w(\eta) &= \sum_{i=1,q,r,s,2} L_i^{(4)}(\eta) w_i \quad , \quad \theta_z(\eta) = \sum_{i=1,2} L_i^{(1)}(\eta)\theta_{zi} - \sum_{j=1,q,r,s,2} M_j^{(3)}(\eta) v_j \end{aligned} \tag{16}$$

where $L_i^{(4)}$ and $M_j^{(3)}$ are Lagrange polynomials and cubic functions, respectively. The beam element developed (named 1^{st}-order element in Ref. [21]) is referred to as 'iTM2D1' in this work (see Fig. 3b). iTM2D1 requires sectional strains from at least three axial sections, leading to a total of at least 18 strain measurements. Consult Appendix A for a complete description of the interpolations functions used.

Additionally, this work also utilises the 0^{th}-order Euler-Bernoulli inverse

element proposed by Savino et al. [24] for slender beams. The element is hereafter referred to as 'iEB2' in this work, and the element formulation is briefly discussed in Appendix B.

2.3 Inverse Beam Element with Warping

In the shape sensing of thin-walled members under torsional deformation, the axial displacements and strains due to warping can negatively affect the estimation of sectional strains when using the inverse elements of Section 2.2, leading to inaccurate iFEM predictions, in particular for open cross-sections. The present section proposes a further improvement to the previous iFEM formulation for the shape sensing of thin-walled structures undergoing combined bending, torsion, and warping deformations.

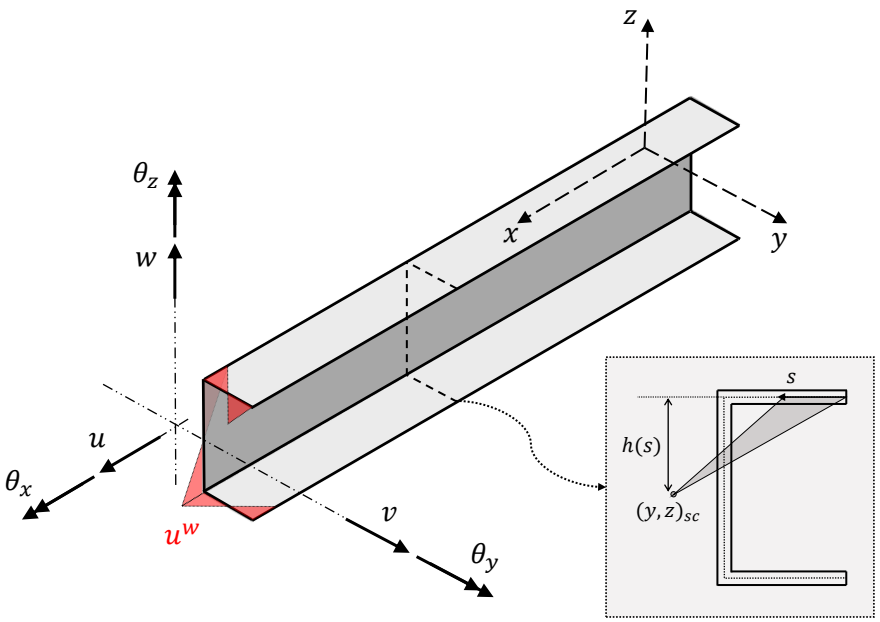

Figure 4: The reference coordinate system and kinematic variables used for defining a thin-walled beam; an illustration of cross-sectional warping (red lines) is also shown

2.3.1 Kinematic Relations

For an open section thin-walled beam warping under torsional loads, the axial displacement along the midline of the flange cross-section is defined as [39]

$$u^w(x,s) = -\omega(s)\theta_{x,x}(x) \tag{17}$$

where $\theta_{x,x}$ represents the rate of twist, and s is the distance measured along the midline of the flange cross-section (see Fig. 4). The function, $\omega(s)$, is the sectorial area defined by the integral [40]

$$\omega(s) = \int_0^s h(s)ds \tag{18}$$

where h is the perpendicular distance from the centre of rotation (shear centre in this case) to the tangent at any point on the flange midline.

The Cartesian components of the displacement vector featuring the additional warping contribution is therefore written as

$$\begin{aligned} u_x(x,s) &= u(x) + z(s)\theta_y(x) - y(s)\theta_z(x) - \omega(s)\theta_{x,x}(x) \\ u_y(x,s) &= v(x) - z(s)\theta_x(x) \\ u_z(x,s) &= w(x) + y(s)\theta_x(x) \end{aligned} \tag{19}$$

The axial and transverse shear strains are derived from Eq. 19 by applying the linear strain-displacement relations

$$\begin{aligned} \epsilon_x(x,s) &= u_{x,x} = e_1(x) + z(s)e_2(x) + y(s)e_3(x) - \omega(s)e_7(x) \\ \gamma_{xz}(x,s) &= u_{x,z} + u_{z,x} = e_4(x) + y(s)e_6(x) - \omega_{,z}(s)e_6(x) \\ \gamma_{xy}(x,s) &= u_{x,y} + u_{y,x} = e_5(x) - z(s)e_6(x) - \omega_{,y}(s)e_6(x) \end{aligned} \tag{20}$$

where e_7 is the sectional strain defined as the second derivative of the torsional rotation and is directly proportional to the axial strain due to warping. The

new analytical sectional strains e_i $(i = 1, ..., 7)$ are written in vector form as

$$\begin{aligned}\mathbf{e}(\mathbf{u}) &= \{e_1, e_2, e_3, e_4, e_5, e_6, e_7\}^T \\ &= \{u_{,x}, \theta_{y,x}, -\theta_{z,x}, w_{,x} + \theta_y, v_{,x} - \theta_z, \theta_{x,x}, \theta_{x,xx}\}^T\end{aligned} \tag{21}$$

2.3.2 Experimental Sectional Strains

Assuming the thin-walled beam is instrumented with strain sensors, Eq. 14 describing the surface strain measurement can be rewritten by introducing an additional contribution due to warping as

$$\begin{aligned}\epsilon^*(x_i, s, \beta) = &\left(e_1^\epsilon(x_i) + e_2^\epsilon(x_i)z(s) + e_3^\epsilon(x_i)y(s) - \omega(s)e_7^\epsilon(x_i)\right)\left(\cos^2\beta - \nu\sin^2\beta\right) \\ &+ \left(\frac{1}{k_{\epsilon z}}e_4^\epsilon(x_i)f_1(s) + \frac{1}{k_{\epsilon y}}e_5^\epsilon(x_i)f_2(s) + e_6^\epsilon(x_i)f_3^w(s)\right)\cos\beta\sin\beta\end{aligned} \tag{22}$$

where $\mathbf{e}^\epsilon \equiv \{e_1^\epsilon, e_2^\epsilon, e_3^\epsilon, e_4^\epsilon, e_5^\epsilon, e_6^\epsilon, e_7^\epsilon\}^T$ are the new experimental sectional strains and f_3^w is the updated shear strain variation function with an additional contribution due to the partial derivatives of ω.

Solution of Eq. 22 requires at least seven strain measurements per section. Also, as e_6^ϵ and e_7^ϵ are coupled quantities, the equations are non-linear and an iterative solution scheme is required. However, the approach can be simplified by assuming an element interpolation order for θ_x. The solution for a quadratic interpolation is discussed here.

For any beam inverse element, the θ_x distribution is defined using the function

$$\theta_x(x) = a_0 + a_1 x + \frac{a_2}{2}x^2 \tag{23}$$

where a_0, a_1 and a_2 are unknown polynomial coefficients. Substituting Eq. 23

in Eq .21 yields the relations for the following sectional strains

$$\begin{aligned} e_6^{\epsilon}(x) &= a_1 + a_2 x \\ e_7^{\epsilon}(x) &= a_2 \end{aligned} \tag{24}$$

Substituting Eq. 24 in Eq. 22 yields the relation

$$\begin{aligned} \epsilon^*(x_i, s, \beta) = &\left(e_1^{\epsilon}(x_i) + e_2^{\epsilon}(x_i) z(s) + e_3^{\epsilon}(x_i) y(s)\right) \left(\cos^2\beta - \nu \sin^2\beta\right) \\ &+ \left(\frac{1}{k_{\epsilon z}} e_4^{\epsilon}(x_i) f_1(s) + \frac{1}{k_{\epsilon y}} e_5^{\epsilon}(x_i) f_2(s)\right) \cos\beta \sin\beta \\ &+ a_1 f_3^w(s) \cos\beta \sin\beta + a_2 (x_i f_3^w(s) \cos\beta \sin\beta - \omega(s)(\cos^2\beta - \nu \sin^2\beta)) \end{aligned} \tag{25}$$

Eq. 25 can be solved using strain measurements from at least two sections with at least six surface strain measurements per section. It should be noted that Eq. 25 offers a specific solution for $\mathbf{e}^{\epsilon}$, i.e., for a quadratic interpolation of θ_x. However, higher order polynomials can also be used depending on the end conditions of the beam and axial variation of torsional strain, e.g. in the case of non-uniform torsion. However, this leads to an increase in the number of unknown coefficients a_i and necessitates additional strain measurements. Such cases are not explored here and are left for future investigations.

2.3.3 Element Interpolations

The interpolation functions for the present beam formulation are similar to those discussed in Section 2.2.3. The only difference is the higher order interpolation for θ_x proposed to solve Eq. 22, which can now be written as

$$\theta_x(\eta) = \sum_{i=1,r,2} L_i^{(2)}(\eta) \theta_{xi} \tag{26}$$

The two beam elements so developed for thin-walled open section beams with warping deformation are hereafter referred to as 'iTM2D0^w' and 'iTM2D1^w'.

3 Experimental Study: C Beam

This section describes a practical application of the 1D iFEM for the displacement reconstruction of a thin-walled prismatic beam using measurements from surface-mounted strain sensors. The experimental data are influenced by imperfections in the applied boundary conditions, uncertainties in the sensor positions, beam geometry, operational environment etc., typically ignored in pure numerical studies (as previously done in Ref. [37]). Hence, the present study offers insight into the accuracy and robustness of the iFEM results obtained. Additionally, the beam is monitored using an optical displacement measurement system based on Digital Image Correlation (DIC), serving as an alternative to strain-based techniques. Comparison with DIC measurements is intended to qualify the advantages and limitations of 1D iFEM against existing or competing strategies. The experimental campaign has been conducted at the LAQ-AERMEC Aeromechanical Structural Systems laboratory (Department of Mechanical and Aerospace Engineering, Politecnico di Torino).

3.1 Experimental Setup

A thin-walled beam with a 'C' cross-section is the specimen chosen for the experimental study. The beam is 1.1 m long, has a section width and height of 30.13 mm $\times$ 45.2 mm, and a flange thickness of 2.08 mm. It is manufactured from an aluminium 6060 alloy with Young's Modulus, $E = 68.03$ GPa, Poisson's ratio, $\nu = 0.335$, and density, $\rho = 2700$ kg/m^3. The beam is tested as a cantilever by clamping the root and applying a concentrated transverse load at the tip. For an effective cantilever condition, roughly half the beam's free length is clamped. Fig. 5 illustrates the beam geometry and its dimensions.

The beam is instrumented with distributed fibre optic strain sensors (FOSS) and strain gauges. The fibre optic sensing (from Luna Innovations) is based on Rayleigh backscatter. It combines a high-definition strain sensor with the ODiSI interrogator system for high-resolution strain measurements at a gauge pitch of

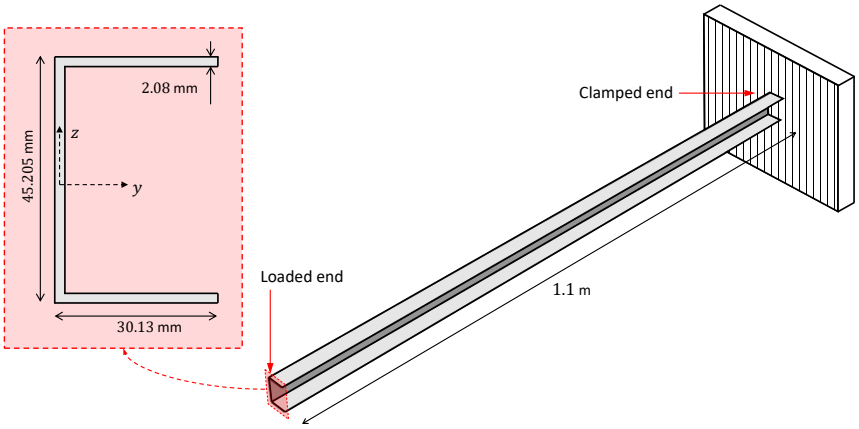

Figure 5: Illustration of the C beam specimen showing the dimensions and boundary conditions (the figure is not necessarily to scale)

1.3 mm and an acquisition frequency of 40 Hz. A 5 m long fibre cable is used and instrumented longitudinally (from the beam root to the tip) to measure strains parallel to the beam axis. The instrumented fibre leads to one strain sensing line per beam flange, with a dense set of strain measurements along each line.

In addition to the fibre optic sensor, strain gauges are used to measure non-axial strains at four axial sections, $x = L/6, L/3, 2L/3$, and $5L/6$ from the beam root (where L is the beam length). Each section is instrumented with three strain gauges, one on each flange and oriented at an angle of 45^0 with the beam axis, for a total of twelve strain measurements. The non-axial strains are required to capture the transverse shear and torsional contribution to beam deformation and are a prerequisite for applying both iTM2D0 and iTM2D1 elements. The axial and cross-sectional locations of the sensors are shown in Fig. 6. Theoretically, iFEM results should be independent of the cross-sectional position of the sensors. However, in a practical context, they might exert an influence. Although discussed in Ref. [37], the present work does not investigate the optimisation of sensor positions. The choice of instrumenting distributed fibre optic sensors on the beam specimen is primarily motivated by the need for a higher density of axial strain measurements for applying the

iEB2 element. For applying the iTM2D0 and iTM2D1 elements, the fibre optic measurements can also be substituted with individual strain gauges without theoretically depreciating the reconstruction accuracy.

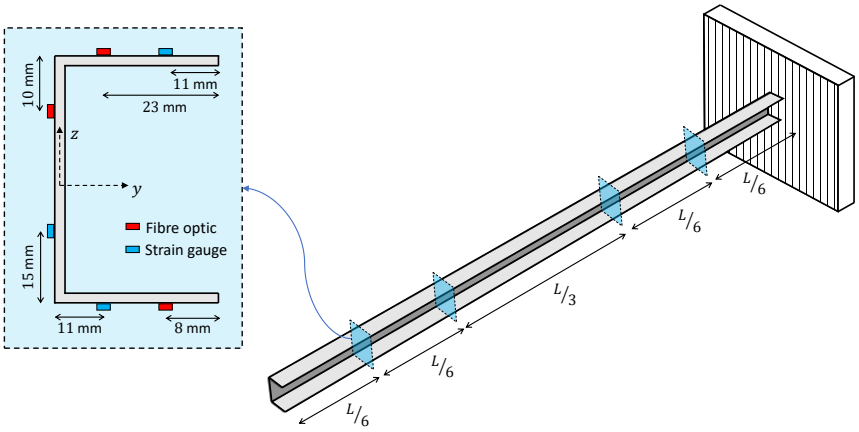

Figure 6: Illustration of the axial and cross-sectional positions of the strain gauges and fibre optic sensors

The beam is loaded at the tip using an assembly of top and bottom plates, and a central core to constrain the tip cross-section, essentially simulating a rib. The loading assembly also allows the load location to be adjusted (with respect to the shear centre) for simulating different beam deformations involving bending and torsion. The beam displacements are measured experimentally only at the tip using two Linear Variable Displacement Transducers (LVDT). The LVDTs are positioned at two ends of the top plate of the loading assembly, and their measurements are used to compute beam tip transverse deflection, w_{sc}, and torsional rotation, $\{\theta_x\}_{\text{sc}}$, at the shear centre,

$$w_{\text{sc}} = w_{\text{LVDT-2}} - \Delta y_{sc} \times \{\theta_x\}_{\text{sc}} \quad , \quad \{\theta_x\}_{\text{sc}} = (w_{\text{LVDT-1}} - w_{\text{LVDT-2}})/\Delta y_{\text{tip}} \tag{27}$$

where Δy_{sc} is the horizontal distance between LVDT-2 and the shear centre, and Δy_{tip} is the horizontal distance between the LVDTs. Images of the experimental setup finally realised in the laboratory are shown in Fig. 7.

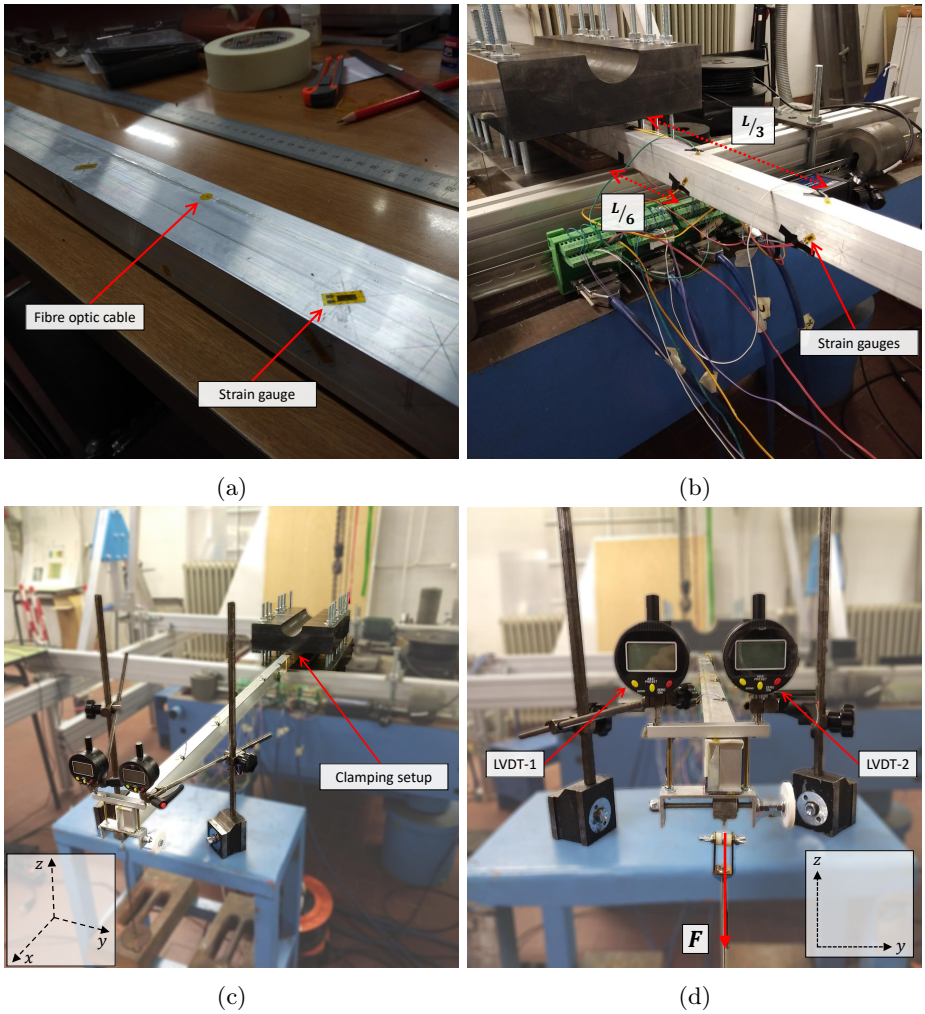

Figure 7: Images of the C beam specimen and the experimental setup in the laboratory: (a) strain sensors instrumented on the beam, (b) beam sections close to the root instrumented with the strain gauges, (c) beam mounted on the clamping setup, and (d) beam loading system and LVDT positions

3.2 Shape Sensing Results

Experimental shape sensing of the C beam is performed using the four inverse beam elements: iEB2, iTM2D0, iTM2D1 and iTM2D0^w. Implementing iTM2D0 and iTM2D1 combines axial fibre optic and non-axial strain gauge measurements. For these elements, the discretisation is a function of the number and location of axial sections instrumented with strain gauges. iTM2D0

and iTM2D1 require experimental sectional strains at two and three axial sections, respectively. Hence, a maximum of two iTM2D0 elements or one iTM2D1 element can be used for the present analysis. The shear coefficients and functions used are provided in Appendix C. Similarly, iEB2 requires experimental sectional strains at two axial sections. However, due to the high-density axial strains measured by the fibre sensor, the beam can be modelled with a variety of coarse and fine iEB2 element discretisation. The element iTM2D0^w is implemented using the same set of strain data as iTM2D1.

Beam loading at the tip is segregated into three load cases defined by the cross-sectional locations of the load applied: at the shear centre ($(y, z)_{sc} = (-11.56, 0)$) and at locations offset from the shear centre. These load cases correspond to torsionless and torsion coupled bending of the beam, respectively, and are described in Table 1. The accuracy of iFEM reconstructed deflections and rotations are evaluated only at the beam tip, coinciding with the location of experimental LVDT measurements.

Table 1: Cross-sectional positions and maximum magnitude of loads applied at the beam tip (defined based on the coordinate system of Fig. 5)

Load case	Load location $(y, z)_F$ (mm)	Maximum load (N)
1	$(-11.56, 0)$	88.3
2	$(15, 0)$	49
3	$(12.5, 0)$	19.6

3.2.1 Results of Load Case 1

Preliminary results for load case 1 are obtained by modelling the beam using one iTM2D1 and up to two iTM2D0 elements, respectively. The number and location of strain measurements used per inverse element are described in Table 2 and 3. Following the initial analysis, the beam is modelled using iEB2 elements with varying fidelities of element discretisation. This preliminary investigation aims to discriminate the shape-sensing accuracy between the three inverse elements.

Table 2: Cross-sectional location (y_s, z_s) and orientation (β) of strain measurements at any axial location (x_s) for iTM2D0, iTM2D1, and iTM2D0^w (coordinate dimensions are in mm and defined based on Fig. 6)

Location coordinates (y_s, z_s)	Orientation (β)
$(6.13, 22.6)$, $(-1.01, 12.5)$, $(21.13, -22.6)$	0^0
$(18.13, 22.6)$, $(-1.01, -7.6)$, $(10, -22.6)$	45^0

Table 3: Axial location (from beam root) and corresponding total number of strain measurements for each inverse beam element

Inverse mesh	Axial location (x_s)	n_{sm}
1 iTM2D0	$\frac{L}{3}$, $\frac{2L}{3}$	12
2 iTM2D0	$\frac{L}{6}$, $\frac{L}{3}$, $\frac{2L}{3}$, $\frac{5L}{6}$	24
1 iTM2D1	$\frac{L}{6}$, $\frac{L}{3}$, $\frac{2L}{3}$, $\frac{5L}{6}$	24
1 iTM2D0^w	$\frac{L}{6}$, $\frac{L}{3}$, $\frac{2L}{3}$, $\frac{5L}{6}$	24

As the beam is loaded approximately at the shear centre, torsional deformation is negligible, and only the transverse tip deflection accuracy is evaluated. The results are shown in Fig 8 where the tip deflection (Fig. 8a) and the corresponding error (Fig. 8b) are plotted as a function of the load applied (where $w^{err} = 100 \times (w_{exp} - w_{\text{iFEM}})/w_{exp}$). For both elements, the reconstructed tip deflection error is less than 10% across all the applied load steps, with one iTM2D1 (average $|w^{err}| \approx 7.5\%$) demonstrating greater accuracy than one iTM2D0 (average $|w^{err}| \approx 8.7\%$). iFEM accuracy also increases with the magnitude of load applied. This is attributed to the higher magnitude of experimentally measured strains and deflections at greater loads which is less susceptible to the influence of noise or measurement errors, thus leading to improved predictions. The use of two iTM2D0 elements leads to results very similar to that of one iTM2D1. The higher accuracy of iTM2D1 is explained by high-order shape functions and the greater number of strain measurements used.

Subsequently, iEB2 elements are also used to model the beam. Due to the high-density axial strains measured by the fibre optic sensor, a variety of element discretisation, from one and up to five equal-length iEB2 elements, are used. The discretisation schemes are selected to avoid strain measurements close

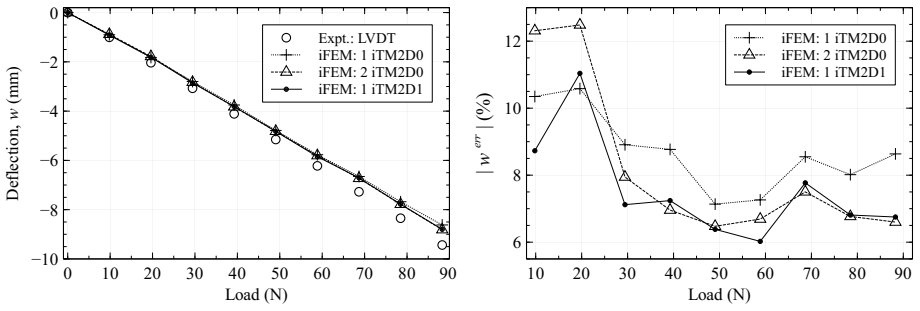

(a) w (b) $|w^{err}|$

Figure 8: iFEM results using iTM2D0 and iTM2D1 compared against experimental measurements (a) tip deflection, w, and (b) deflection error , w^{err}, at the shear centre as a function of the load applied

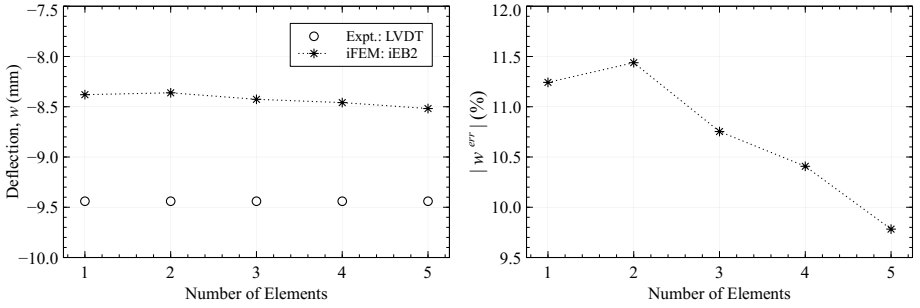

(a) w (b) $|w^{err}|$

Figure 9: iFEM results obtained using iEB2 elements for a tip load of 88.3 N compared against experimental measurements (a) tip deflection, w, and (b) deflection error, w^{err}, at the shear centre as a function of the number of inverse elements used

to the clamped or free end of the beam (to avoid strain data influenced by end effects) and use experimental sectional strains computed at two axial sections within each element. The iEB2 elements are used to analyse beam deformations produced by a tip load of 88.3 N, and the results are shown in Fig. 9.

The reconstructed tip deflection converges to the reference value as the number of inverse elements used increases (shown in Fig. 9a). As element discretisation becomes more refined, the strain and displacement distribution along the beam can be modelled more accurately, resulting in better iFEM predictions. The tip deflection error reduces from ∼11.2% when using one to ∼9.7% for five iEB2 elements (see Fig. 9b). Further increase in the inverse mesh discretisation

is expected to produce smaller increments in tip deflection accuracy, eventually converging to a specific value.

Table 4: Comparing element accuracy for load case 1 at the final load step

Inverse mesh	n_{sm}	w_{tip} (mm)	$\lvert w^{err} \rvert$ (%)
Experimental	–	−9.43	–
1 iEB2	6	−8.38	11.24
1 iTM2D0	12	−8.62	8.63
2 iTM2D0	24	−8.81	6.60
1 iTM2D1	24	−8.79	6.75
1 iTM2D0^w	24	−8.67	8.09

iFEM results using the different inverse elements demonstrated increasing levels of accuracy from $|w^{err}| \approx 11.2\%$ for one iEB2 element to $|w^{err}| \approx 6.7\%$ for one iTM2D1 element. The differences in the results are related to the element formulations, where the treatment of transverse shear deformation and order of interpolation functions used for each element are different. This is the case for iTM2D0 and iTM2D1, as they capture both transverse shear and torsional deformations. Despite the higher-order shape functions of iTM2D1, the difference in accuracy with iTM2D0 is insignificant, indicating the linear interpolation of the bending curvatures (in the case of iTM2D0, while for iTM2D1, it is parabolic) to be consistent and sufficient for the tip loaded cantilevered beam problem investigated. In contrast, the lower tip deflection accuracy for iEB2 is consistent with the absence of transverse shear deformation in its results. Increasing the fidelity of discretisation is a strategy for improving iTM2D0 and iEB2 predictions, as demonstrated successfully in Figs. 8 and 9. A comparison of results between the elements for the final load step is provided in Table 4, where it is seen that the use of the iTM2D0^w element produced no significant improvement over the high accuracy reported using the other elements. This is attributed to the absence of torsional and warping deformation in load case 1, indicating perhaps it is not best suited for pure bending applications.

However, the accuracy of each element should be qualified considering the number of in-situ strain measurements required per element. iEB2, iTM2D0,

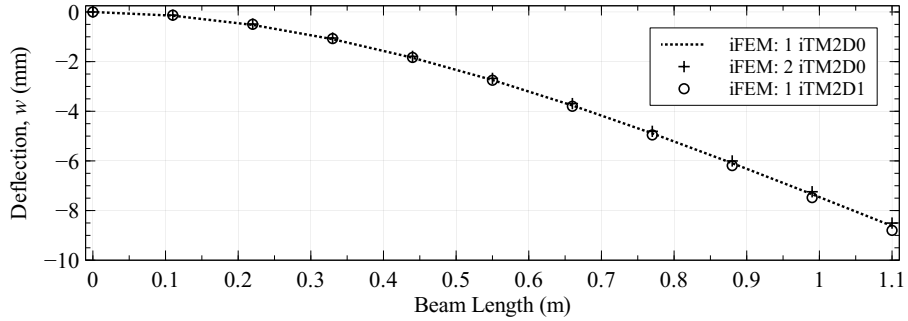

(a)

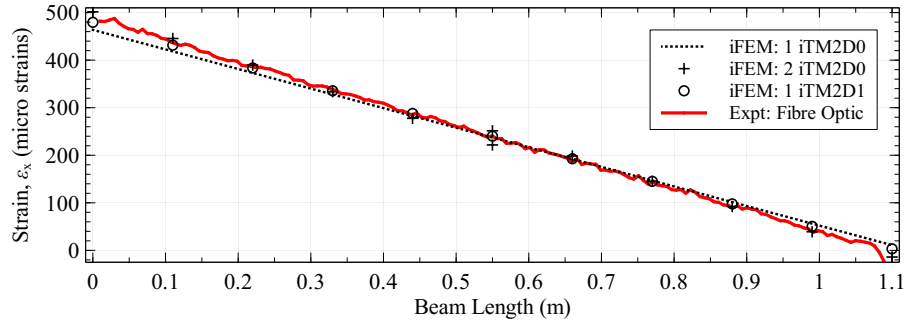

(b)

Figure 10: iFEM results along the beam length for load case 1: (a) deflection and (b) longitudinal strains on the top flange for a tip load of 88.3 N

and iTM2D1 require a minimum of 6, 12 and 18 strain measurements per element, respectively. It also increases with the fidelity of the discretisation scheme, with a corresponding increase in computational effort. In conclusion, iTM2D0 provides an optimal trade-off between high reconstruction accuracy and low sensor requirement for the present shape sensing problem. These results serve as an experimental validation of the iTM2D0 and iTM2D1 element formulations, specifically for accurately modelling the contribution of transverse shear to the beam deformation. In addition to these results, Figs. 10a and 10b compare the iFEM deflection and strains along the entire length of the beam, reconstructed using the Timoshenko inverse elements discussed in this section.

3.2.2 Results of Load Case 2

The torsional deformation of the beam gains prominence with an increase in distance between the load location and the shear centre. In the present case, the load is applied approximately midway to the horizontal flange (~ 26.56 mm from the shear centre). The maximum load applied is also reduced (49 N as given in Table 1) to limit the additional stresses due to beam torsion. Similar to load case 1, the inverse model of the beam is discretised using one iTM2D1 and up to two iTM2D0 elements with sensor positions given in Tables 2 and 3.

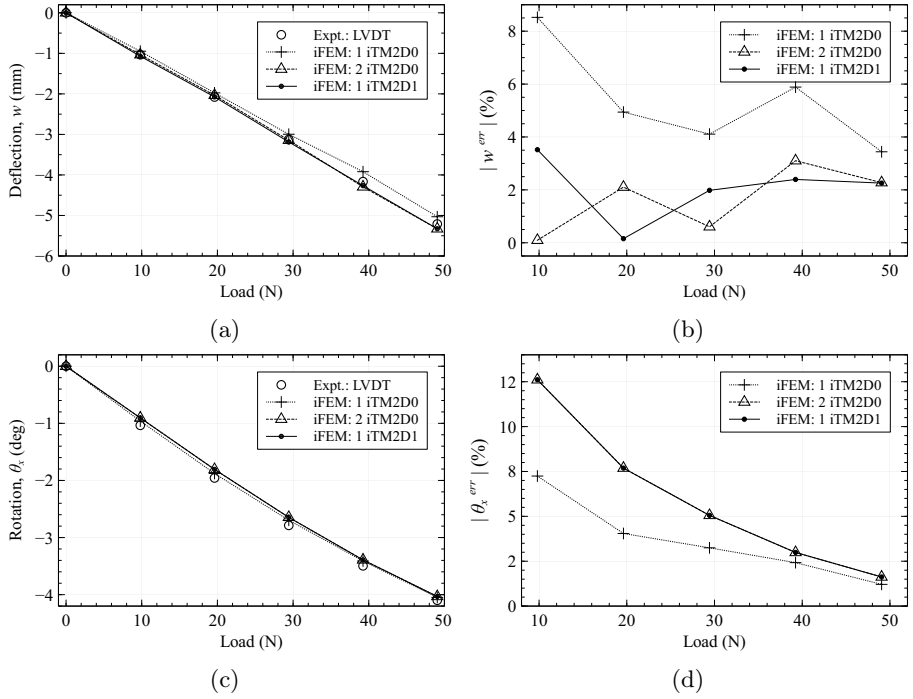

Figure 11: iFEM results using one iTM2D0 element compared with experimental measurements: (a) tip deflection, w, (b) deflection error, w^{err}, (c) tip torsional rotation, θ_x, and (d) rotation error, θ_x^{err}, at the shear centre as a function of the load applied

As the beam undergoes combined bending and torsional deformation, the experimental LVDT measurements are used to compute the transverse deflection of the shear centre of the beam (see Eq. 27). The reconstructed tip deflection, plotted in Fig 11a, is seen to be very accurate with a maximum error less than 3.5% at the final load step (as shown in Fig 11b), proving consistent

Table 5: Comparing element accuracy for load case 2 at the final load step

Inverse mesh	n_{sm}	w_{tip} (mm)	$\lvert w^{err}\rvert$ (%)	$\theta_x\rvert_{tip}$ (deg)	$\lvert\theta_x^{err}\rvert$ (%)
Experimental	–	−5.21	–	−4.09	–
1 iTM2D0	12	−5.03	3.44	−4.05	1.21
2 iTM2D0	24	−5.33	2.27	−4.03	1.62
1 iTM2D1	24	−5.33	2.25	−4.03	1.62
1 iTM2D0^w	24	−5.27	1.26	−3.97	3.05

with load case 1 results. In contrast, accurately reconstructing the torsional deformation poses the main challenge for the present problem. However, Fig. 11c demonstrates the high accuracy of iTM2D0 and iTM2D1 in reconstructing torsional tip rotation, with an error less than ∼3% at the final two load steps (see Fig. 11d). The use of iTM2D0^w is seen to improve the prediction of w, while diminishing θ_x reconstruction accuracy, indicating a possible trade-off due to the bending-torsion coupling present in the estimation of the sectional strains. However, the change in error is only marginal, given the already high shape sensing accuracy reported using the other elements. A comparison of displacement results between the elements for the final load step is provided in Table 5, while plots of the iFEM reconstructed deflections and strains along the beam length is provided in Figs. 12b and 12b.

An accurate reconstruction of torsional rotation is predicated on an accurate estimation of the experimental sectional strain corresponding to the rate of twist (e_6^ϵ using Eq. 14), and the present results serve to provide a conclusive validation of the iFEM formulation. These results demonstrate the 1D iFEM to be an accurate and efficient approach for the shape sensing of beams undergoing combined bending, transverse shear, and torsional deformations.

3.3 Comparison with DIC Measurements

Evaluation of iFEM accuracy in Section 3.2 is performed only at the beam tip as LVDTs are point displacement measurement instruments. Comparing iFEM results with other commercial contact or non-contact measurement systems that

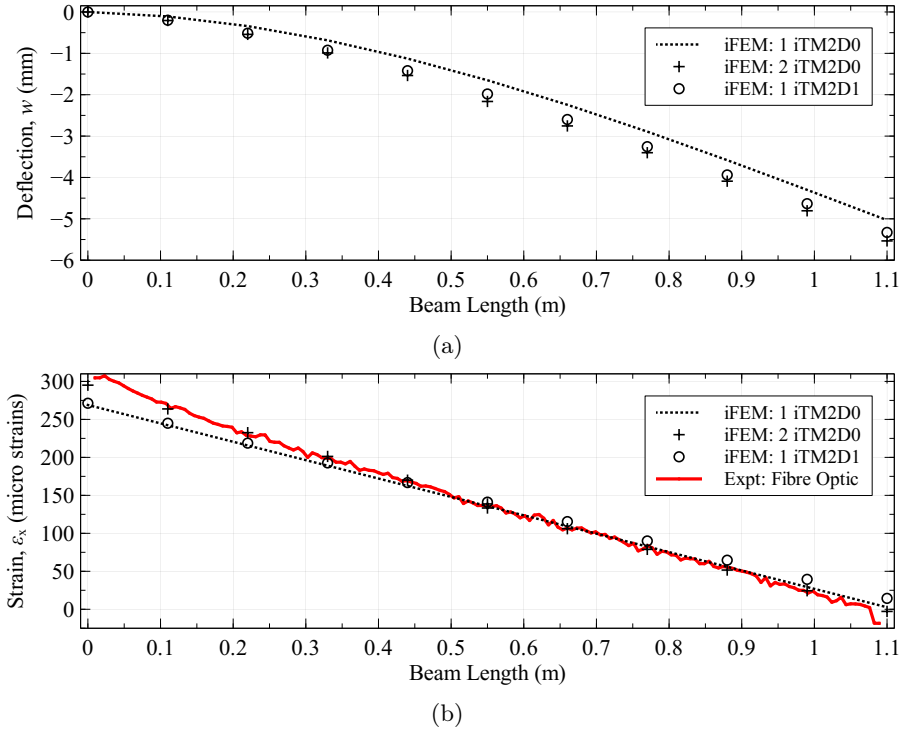

Figure 12: iFEM results along the beam length for load case 2: (a) deflection and (b) longitudinal strains on the top flange for a tip load of 49 N

measure structural displacements over a larger portion of the structure can reveal additional nuances in the iFEM predictions. For such a comparison, the VIC-3D system, based on DIC and offered by Correlated Solutions, is used to monitor the beam. The VIC-3D system comprises of high-resolution digital cameras for image acquisition and a DIC software for analysing the captured images and computing the deformation and strain on the structure. In contrast to an LVDT, the DIC system offers a significantly higher density of measurement points over the monitored area and computes real-time 3D displacements and strains at each point.

The size of the structural area monitored by the VIC-3D system is a function of the camera resolution, specimen size, measurement precision etc. For the present experiment, a 95.5×41 mm^2 rectangular area on the vertical flange of the beam is monitored, as shown in Fig. 13. A transverse tip load of 19.6 N is

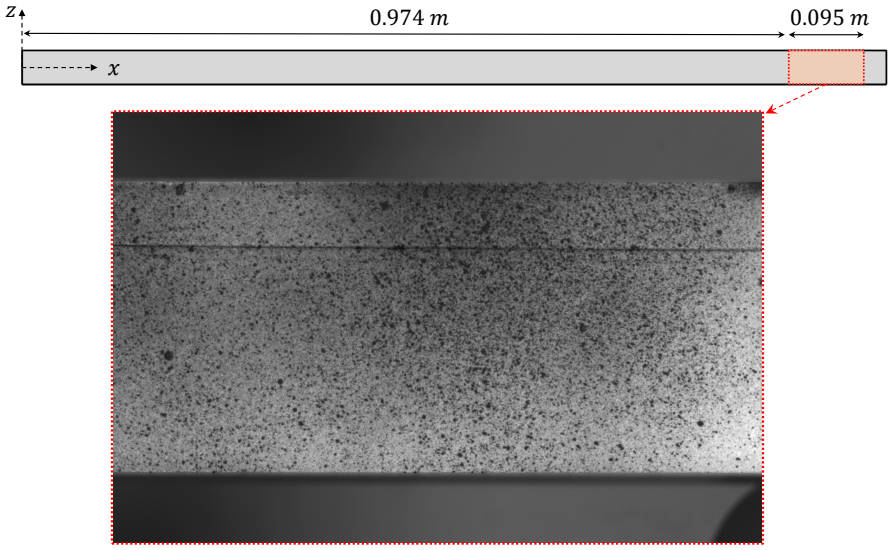

Figure 13: Beam surface on the vertical flange monitored using the VIC-3D system (a dense grid of points can be seen on the surface)

applied based on load case 3 (see Table 1), and VIC-3D is used to measure both in-plane (u_x and u_z) and out-of-plane (u_y) displacements on the beam surface. Contour plots of these measurements are shown in Figs. 14a, 14c, and 14e. Due to the nature of the applied loading, the beam undergoes both bending, as seen from the linear variation of u_x along the $z-$axis, combined with torsion, as u_z is no longer a constant at each axial section. Among the transverse displacements, u_z is predominant (over one order of magnitude greater than u_y) and hence is given more priority when assessing the iFEM results.

The inverse model of the beam is composed of one iTM2D1 element and uses the in-situ strain measurement locations outlined in Tables 2 and 3. The displacement field over the monitored area is computed from the reconstructed nodal displacements using the shape functions (see Eq. 16) and kinematic relations of the beam element (see Eq. 10). The iFEM reconstructed displacement field is shown in Figs. 14b, 14d and 14f. A cursory comparison of the plots reveals the iFEM results to be accurate in terms of magnitude and distribution. The sole exception is the displacement along the unloaded transverse axis (u_y), which is expected to be the most susceptible to measurement noise or errors.

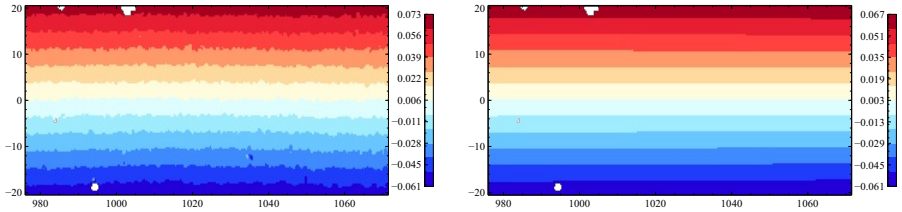

(a) $u_x|_{\text{VIC-3D}}$ (b) $u_x|_{\text{iFEM}}$

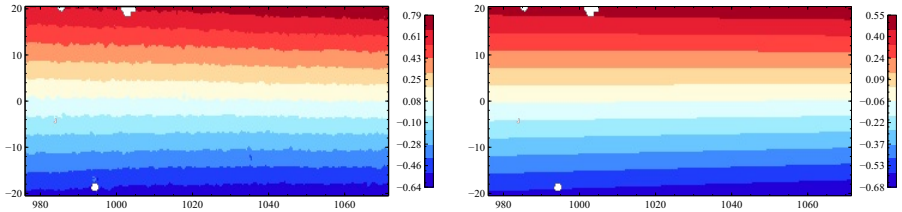

(c) $u_y|_{\text{VIC-3D}}$ (d) $u_y|_{\text{iFEM}}$

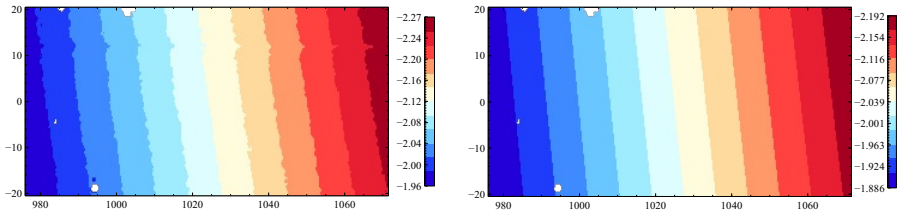

(e) $u_z|_{\text{VIC-3D}}$ (f) $u_z|_{\text{iFEM}}$

Figure 14: Contour plots of VIC-3D measurements and iFEM reconstructed displacements where the origin of the horizontal coordinate, x, is the beam root, and that of the vertical coordinate, z, is the flange midpoint (all dimensions and displacement values are in mm)

Given the high spatial density of VIC-3D measurements, the percentage difference or error in iFEM reconstructed displacement at each measurement point is also computed. Aggregating all points leads to the error contour plots of Fig. 15.

The contour of plot u_z^{err} (see Fig. 15c) demonstrates the transverse displacement reconstruction to be accurate with a maximum error of $\sim$4%. As u_z is computed based on the iFEM reconstructed nodal w and θ_x values, the accuracy of the former demonstrates those of the latter two as well. The horizontal line across the plot coincides with the fibre optic sensor instrumented on the beam flange, highlighting the high spatial density of VIC-3D measurements. Simi-

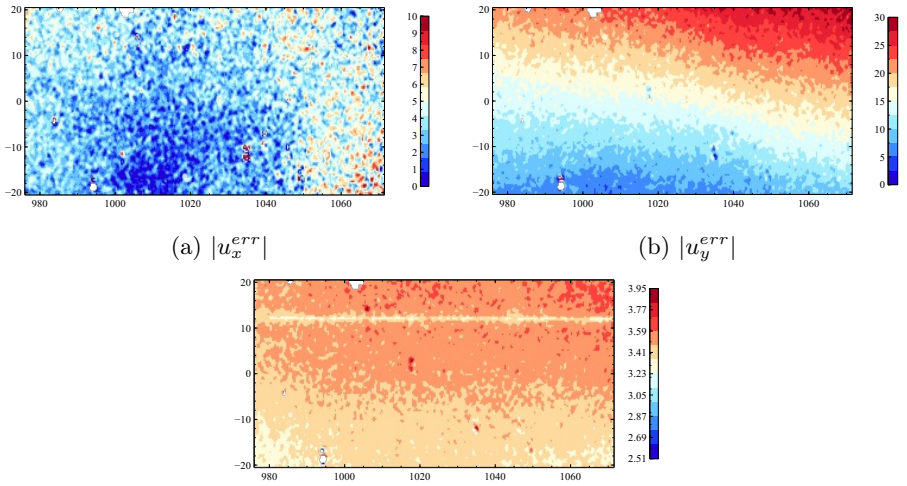

(a) $|u_x^{err}|$ (b) $|u_y^{err}|$

(c) $|u_z^{err}|$

Figure 15: Contour plots of percentage difference (absolute value) in VIC-3D measurements and iFEM reconstructed displacements: (a) $|u_x^{err}|$, (b) $|u_y^{err}|$, and (c) $|u_z^{err}|$, over the monitored area of the beam flange

larly, u_x reconstruction is also observed to be accurate over the majority of the monitored area (with an error less than 5%, as shown in Fig. 15a). However, the plot is also populated with several error peaks (with a maximum of ∼10%). These peaks are attributed to the low magnitude of u_x combined with errors in the experimental measurements, surface treatment, etc. As observed in Fig. 14d, u_y results are inaccurate with a maximum error of ∼30% (see Fig. 15b).

The accuracy of u_x and u_z reconstructions reinforce the ability of iTM2D1 to reconstruct bending, transverse shear, and torsional deformations of the beam accurately. The experimental campaign also demonstrated several limitations of the VIC-3D system, including high equipment cost, camera resolution and distance from the beam influencing the size of the structural area that can be monitored, the influence of surface treatment on DIC results, initial system calibration, etc. In comparison, iFEM can reconstruct full-field displacements and rotations in real-time using information regarding structural geometry and a sparse set of strain sensors. These studies demonstrate iFEM as an accurate and efficient alternative to optical-based displacement measurement techniques.

4 Experimental Study: Airfoil Beam

Building on the success of previous results, the 1D iFEM is further applied for the shape sensing of beams with more complex cross-sections. The structure analysed in this section is a thin-walled beam with a symmetric airfoil cross-section (NACA 0016), as shown in Fig. 16. The original beam profile is slightly modified, with the sharp airfoil trailing edge rounded or chamfered for practical convenience. The beam is additively manufactured by Direct Metal Laser Sintering (DMLS), as other conventional manufacturing approaches would have proved inefficient for such complex geometries.

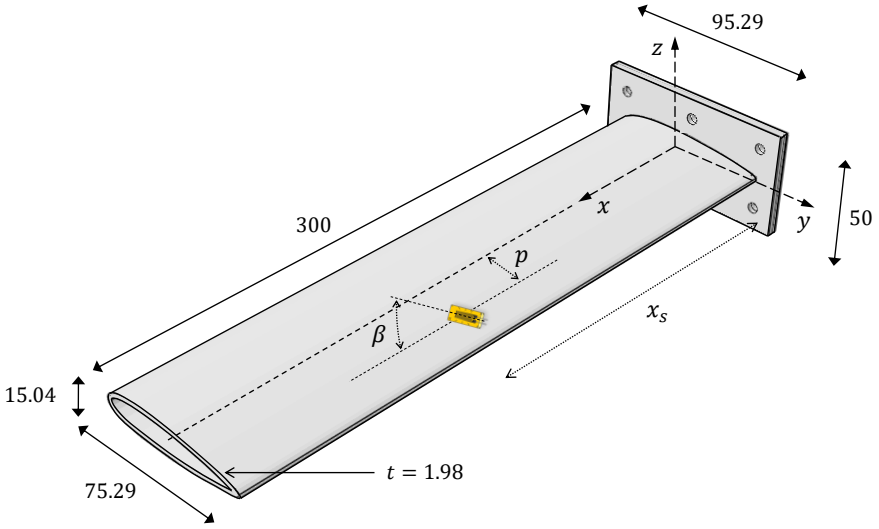

Figure 16: Illustration of the thin-walled airfoil beam ($t = 1.98$ mm) with the dimensions and the clamping flange shown (all dimensions are in mm)

4.1 Experimental Setup

Although designed to be tested as a cantilever, limitations on specimen size imposed by the manufacturing process required the adoption of an alternative beam root clamping strategy (compared to that in Section 3). In this case, a clamp condition is approximated by printing a flange at the beam root. The flange is to be subsequently connected to an external solid support using clamp-

ing bolts. This strategy is assessed using a high-fidelity FEM beam model developed in ABAQUS. The numerical results revealed negligible axial displacement and bending rotation at the beam root, thus approximating a fixed condition.

Table 6: Material properties of the aluminium alloy used.

Material	Young's modulus (GPa)	Density (kg/m^3)	Yield strength (MPa)	Strain at break (%)
AlSi10Mg	70 ± 10	2670	240 ± 30	6 ± 5

The beam is manufactured of an aluminium alloy (AlSi10Mg) with material properties reported in Table 6. A key limitation of additive manufacturing is that the printed specimen is influenced by print parameters such as feed rate, layer thickness, part orientation, and the resulting local heating and cooling cycles experienced by the part. Hence, the material behaviour is also influenced by the part geometry, with local properties differing from those obtained through tensile tests (reported in Table 6). Due to the novel manufacturing approach adopted and its associated uncertainties, a high safety factor (~ 10) is used at the design stage.

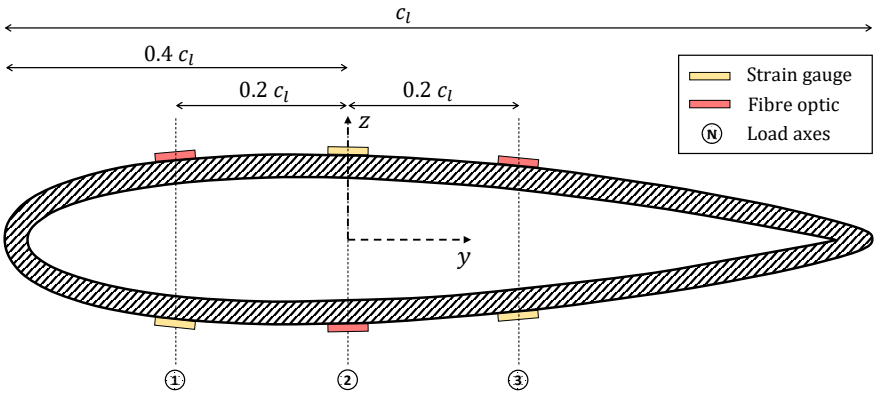

Figure 17: Location of the sensors and applied load ($c_l = 75.29$ mm)

The beam is loaded at the tip using a loading system composed of top and

bottom flanges and an inner core, effectively simulating a rib. It is loaded incrementally, with load steps of 4.9 N, up to a maximum load of 49 N. The loads can be applied transversally at three chord-wise locations of the beam (as shown in Fig. 17) to simulate both bending and torsional deformations. Experimental deflections are measured using LVDTs positioned on either side of the top flange (of the loading setup). Similar to the experimental tests of Section 3, the airfoil beam is also instrumented with 15 strain gauges and a 2 m long distributed fibre optic sensor. The locations of these sensors on the beam cross-section are shown in Fig. 17. Images of the printed beam, loading system, instrumented sensors, and the experimental setup are shown in Figs. 18.

The notation $[p^{\pm}, x_s, \beta]$ [37] is used to define the exact position and orientation of sensors or strain measurements on the beam surface (see Fig. 16). Parameters x_s and β are the sensor distance from the beam root and orientation with respect to the beam axis, respectively. At any axial beam section x_s, the parameter p is the distance from the beam centroid, measured parallel to the airfoil chord line and normalised with respect to the local chord length. The superscripts $+$ and $-$ represent sensors placed on the airfoil's upper or lower surface. The inverse beam models analysed and the corresponding sensor configurations used are described in Table 7.

Table 7: The inverse meshes and the corresponding sensor configurations used for the iFEM analysis

Inverse meshes	n_{sm}	Sensor configuration (p, x_s, β)
1 EB2 / 1 iTM2D0 / 1 iTM2D1	24	$[(\pm 0.2^{+}, 0^{-}), (\frac{L}{6}, \frac{L}{3}, \frac{L}{2}, \frac{2L}{3}), 0.0]$ $[(\pm 0.2^{-}, 0^{+}), (\frac{L}{6}, \frac{L}{3}, \frac{L}{2}, \frac{2L}{3}), 45]$

4.2 Preliminary Shape Sensing Results

The iFEM results using one iEB2 element for the beam loaded approximately through the shear centre (along axes 2 of Fig. 17) is shown in Fig. 19a. The iFEM results are widely inaccurate, with a percentage error approaching $\sim$50%

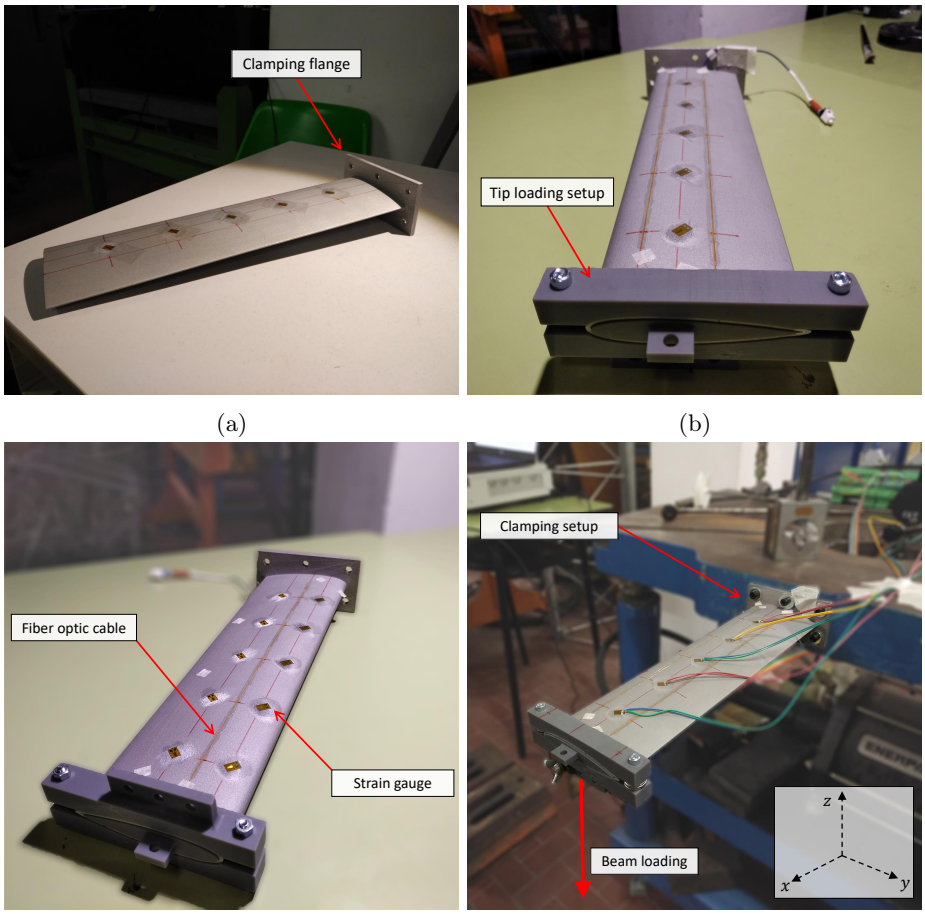

Figure 18: Images showing (a) the final printed beam specimen, (b) the loading system at the beam tip, (c) the beam instrumented with strain sensors, and (d) the beam tested on the experimental setup

at the final load step (see Fig. 19b). The inaccuracy could be attributed to errors in the iFEM formulation and its potential unsuitability for analysing the present structure. It could also be an inconsistency between the intended and practically realised experimental setup. This latter hypothesis is investigated by computing the analytical beam deflections based on Timoshenko theory (see Fig. 19a). The similarity between analytical and iFEM results highlights an issue with the specimen or test setup. The linear behaviour of both displacement and strains rule out the effect of material or geometrical non-linearities. Additionally, as the deflection error varies linearly with the load applied, a linear elastic phenomenon

can explain the present behaviour.

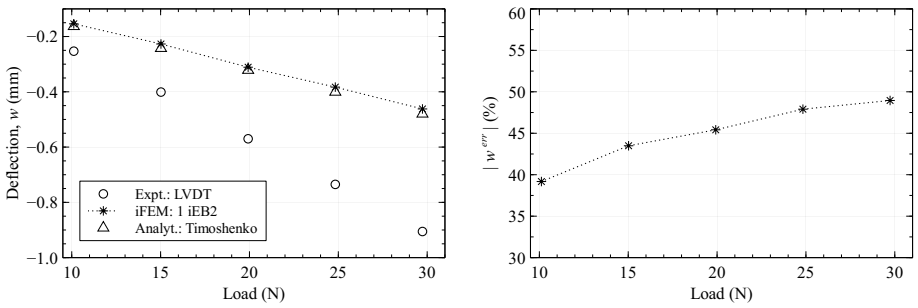

(a) (b)

Figure 19: Comparison of experimental, iFEM (using one iEB2 element), and analytical results: (a) tip deflection and (b) percentage error (iFEM with respect to LVDT), as a function of the load applied

A closer inspection revealed imperfect clamping, resulting from a crack at the intersection of the beam and the flange, to be the issue (shown in Fig. 20). The crack is shallow and extends from the leading edge to the mid-chord of the airfoil on both upper and lower surfaces. Crack opening and closing during beam loading produces rigid body rotation and introduces an additional linear component of transverse deflection along the beam. Hence, the assumption of a fixed root boundary condition in the inverse model is incorrect. The beam failure could be due to the imperfect realisation of the specimen at the beam-flange interface. During the manufacturing process, the effect of local heating and cooling cycles at this critical site (where there is a sudden change in beam section) can lead to much lower mechanical properties than those reported in Table 6. To verify this conclusion, a high-fidelity finite element model of the airfoil beam was developed in ABAQUS. The beam was meshed using 9440 S4R shell elements and the external constraints on nodes at the beam root (i.e., the clamped end) was modified to simulate cracks of varying lengths. The experimental data are compared with the FE predictions in Fig. 21, where a crack extending from the leading edge (over the upper surface) to nearly 70% the chord length produced displacement results consistent with those measured. The strain variation near the damage was also similar and a more precise definition of the actual damage

is required to achieve greater correlation.

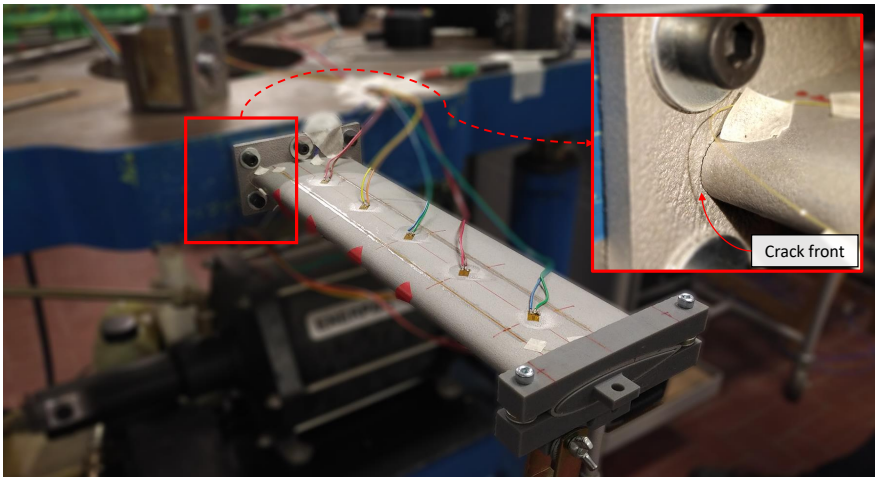

Figure 20: The damage location on the beam; the inset shows the crack formed along the beam leading edge

Similar to the numerical model discussed, an analytical model of the beam is also developed. The damaged specimen, in this case, can be modelled as an elastic spring-hinged cantilever beam. The spring stiffness is a function of the crack length and width, i.e., it tends to infinity as it approaches a perfect clamp condition. The analytical deflection equation for such a beam can be written as a superposition of a rigid-body, w_{rb}, and elastic (computed based on Timoshenko beam theory), w_{tim}, contribution as

$$\begin{aligned} w(x) &= w_{rb}(x, K_r) + w_{tim}(x) \\ &= \left(\frac{F_z L}{K_r} x\right) + \left(\frac{F_z L}{2EI_{yy}} x^2 - \frac{F_z}{6EI_{yy}} x^3 + \frac{F_z}{AGk_{tz}} x\right) \end{aligned} \tag{28}$$

where F_z is the transverse tip load along the $z-$axis, K_r is the spring stiffness, and k_{tz} is the classical shear correction factor of the beam profile. As iFEM captures the elastic deformation of the beam, it can be accurately compared with w_{tim} of Eq. 28. The next section explores this possibility by introducing a filtering approach to remove the rigid-body contribution from the experimental displacement measurements.

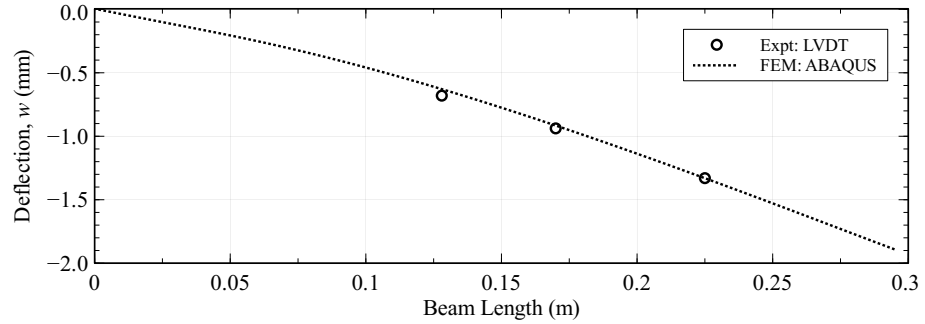

(a)

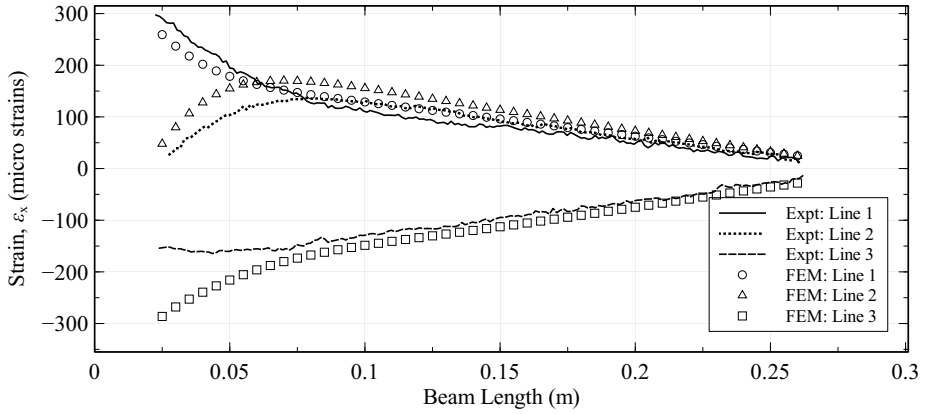

(b)

Figure 21: Comparison of FEM predicted (a) deflection and (b) longitudinal strains (along different fibre optic sensing lines), against experimental results of the damaged airfoil beam for a tip load of 49 N

4.3 Filtering Experimental Data

The direct filtering of measured displacements to obtain only the contribution due to beam deformation requires prior knowledge of the spring stiffness, material properties, and applied loads. As an accurate model of the beam in its damaged state is unavailable, an inverse filtering approach is used instead. Based on Eq. 28, the beam displacements can be described as

$$w(x) = c_1 x + c_2 \left(x^2 L - \frac{x^3}{3} + x \frac{4(1+\nu) I_{yy}}{A k_{tz}} \right) \tag{29}$$

where $c_1 = \frac{F_z L}{K_r}$ and $c_2 = \frac{F_z}{2EI_{yy}}$ are constants that are a function of the spring stiffness, material, and loading conditions.

In the inverse context, constants c_1 and c_2 are assumed to be unknowns that are computed from experimental measurements. For displacements measured experimentally at n axial locations $x = x_1,...,x_n$ of the beam ($n \geq 2$), Eq. 29 can be expanded and written as

$$\begin{Bmatrix} w(x_1) \\ \vdots \\ w(x_n) \end{Bmatrix}_{exp} = \begin{bmatrix} x_1 & x_1^2 L - \frac{x_1^3}{3} - x_1 d_1 \\ \vdots & \vdots \\ x_n & x_n^2 L - \frac{x_n^3}{3} - x_n d_1 \end{bmatrix} \begin{Bmatrix} c_1 \\ c_2 \end{Bmatrix} \tag{30}$$

where $d_1 = \frac{4(1+\nu)I_{yy}}{Ak_{tz}}$ is a constant for the beam geometry. Eq. 30 is further described in vector form as

$$\mathbf{u}_{exp} = \mathbf{A}\mathbf{c} \tag{31}$$

where $\mathbf{u}_{exp}$ is a vector of experimental displacement measurements, $\mathbf{c}$ is the vector of unknown constants, and $\mathbf{A}$ is a function of the geometric properties and Poisson's ratio of the beam ($\nu \approx 0.3$ for metallic materials).

As Eq. 31 is ill-posed (especially when using experimental data), it is formulated in terms of a regularised least-squares problem [41] and solved to obtain the unknown coefficient vector using

$$\mathbf{c} = (\mathbf{A}^T\mathbf{A} + \alpha\mathbf{I})^{-1}\mathbf{A}^T\mathbf{u}_{exp} \tag{32}$$

where $\mathbf{I}$ is a $n \times n$ identity matrix and α is the regularisation parameter used to obtain accurate solutions when using noisy displacement measurements.

The filtered displacements, $\mathbf{u}_f$, can now be obtained by

$$\mathbf{u}_f = \mathbf{u}_{exp} - c_1\mathbf{x} \approx \mathbf{u}_{tim} \tag{33}$$

where $\mathbf{x}$ is the vector of axial coordinates of the measurements and $w_{rb} \approx c_1\mathbf{x}$

is the filtered rigid-body contribution.

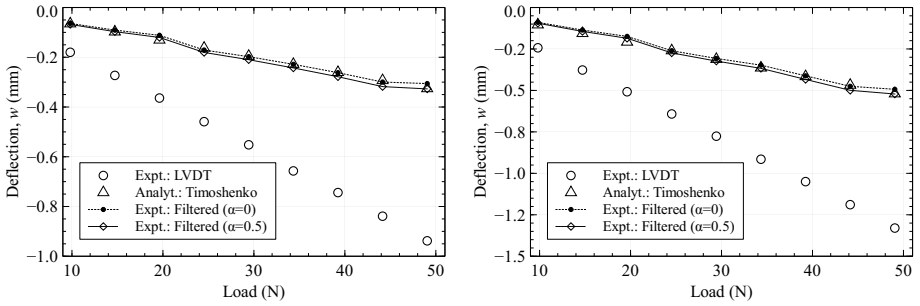

Figure 22: The experimental, analytical, and filtered beam deflections at (a) $x = 170$ mm and (b) $x = 225$ mm as a function of the load applied

Table 8: Comparison of experimentally measured, analytical, and filtered deflections at $x = 225$ mm for different regularisation values

Load (N)	w_{exp} (mm)	w_{tim} (mm)	$w_f\|_{\alpha=0}$ (mm)	$w_f\|_{\alpha=0.5}$ (mm)
9.8	−0.243	−0.103	−0.089	−0.094
19.6	−0.508	−0.207	−0.174	−0.185
29.4	−0.776	−0.311	−0.307	−0.323
39.2	−1.050	−0.415	−0.411	−0.433
49.0	−1.330	−0.519	−0.493	−0.521

4.4 Updated Shape Sensing Results

The displacement filtering strategy is applied for the airfoil beam problem using LVDT measurements from three axial locations of the beam: x =128, 170, and 225 mm. For the case when the beam is loaded through the shear centre up to a maximum load of 49 N, the filtered displacement results are shown in Fig. 22 and reported in Table 8. The filtered displacements correlate very well with the analytical results. Furthermore, a comparison of iFEM predictions using one iEB2 element compared against the filtered displacements is shown in Fig. 23a.

Although the original measurements are still widely inaccurate, the iFEM results and the filtered displacements correlate very well. The conclusions are better represented by the error plots of Fig. 23b where $w^{err} < 10\%$ for loads greater than 20 N is similar to the iEB2 accuracy seen in Section 3.2. The

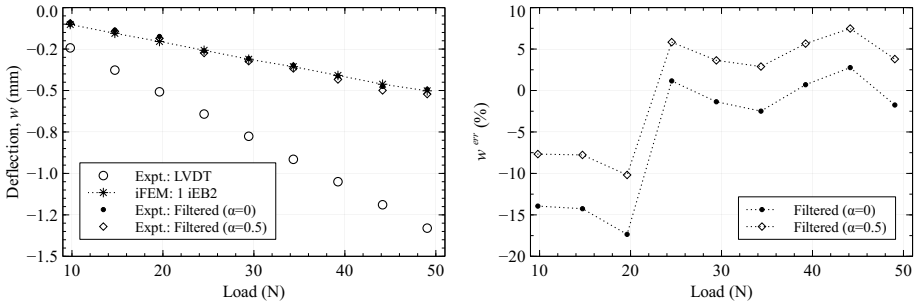

(a) (b)

Figure 23: iFEM results using one iEB2 element compared against filtered and unfiltered measurements at $x = 225$ mm: (a) transverse deflection, and (b) percentage error as a function of the load applied

inaccuracies observed for loads less than 20 N are attributed to the sensitivity of the filtering strategy to noise and can also be seen as the slight non-linearities in Figs. 22 and 23a. Additionally, the regularisation term is also seen to have an impact with filtering using $\alpha = 0.5$ better modelling analytical Timoshenko displacements (see Table 8).

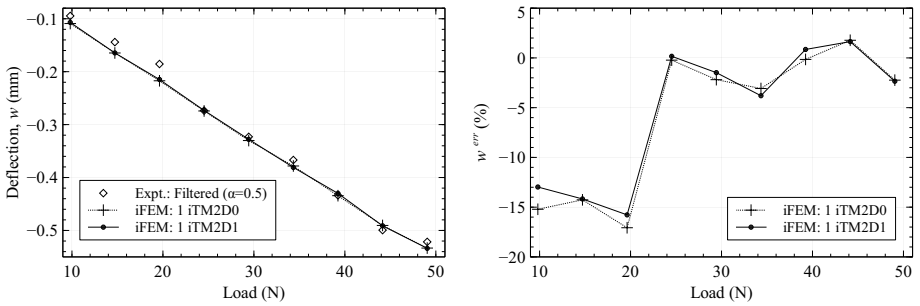

(a) (b)

Figure 24: iFEM results using one iTM2D0 and one iTM2D1 element compared against filtered measurements at $x = 225$ mm: (a) transverse deflection, and (b) percentage error as a function of the load applied

The airfoil beam is also modelled with one iTM2D0 and one iTM2D1 element using strains based on Table 7. The shear coefficients and functions used for the analysis are given in Appendix C. Due to the additional transverse shear deformation modelled by these elements, iFEM results are compared against $w_f|_{\alpha=0.5}$ and are shown in Fig 24. Similar to the previous comparison, iTM2D0

and iTM2D1 results are very accurate with $w^{err} < 5\%$ for loads greater than 20 N, with very little difference between the two elements. The iFEM results for the airfoil beam at the final load step are tabulated and compared in Table 9. The accuracy for all three inverse elements is quite similar to those reported in Section 3.2, with iEB2 proving to be the least and iTM2D0 or iTM2D1 the most accurate.

Table 9: Comparison of iFEM against $w_f|_{\alpha=0.5}$ at the final load step

Mesh	$x = 128$ mm		$x = 170$ mm		$x = 225$ mm	
	w (mm)	w^{err} (%)	w (mm)	w^{err} (%)	w (mm)	w^{err} (%)
1 EB2	−0.186	15.05	−0.311	4.94	−0.501	3.79
1 iTM2D0	−0.204	6.93	−0.334	−2.31	−0.533	−2.23
1 iTM2D1	−0.215	2.22	−0.342	−4.77	−0.533	−2.34

Despite the success of these comparisons, the filtering results obtained are influenced by the value of α used. In this context, developing more robust filtering strategies is expected to improve the accuracy of these comparisons further. Additionally, investigations on using 1D inverse elements to analyse beams with material and geometrical non-linearities are a further step in maturing the technology. In the latter case, 1D iFEM can be applied based on the incremental formulation of Tessler et al. [42] to reconstruct large non-linear beam deformations. Alternatively, the thin-walled beam in the present problem can be modelled using inverse shell elements [13] with problem-specific constraints applied at the root to model the damage. However, the applicability of this strategy is also limited because damaged strains at the root are highly localised and a greater number of strain sensor measurements are required to capture their accurate distribution. Strain smoothing techniques [43, 44] can be used to augment the number of strain measurements and could offer a limited solution in the present case. Additionally, despite the reported efforts, the exact nature of the mesh and constraints required to represent the damage are still unknown and can only be resolved by more accurate beam characterisation.

These efforts are outside the scope of the present work, but would certainly be an interesting topic for future investigations.

5 Conclusions

This work presented an inverse methodology, based on the 1D iFEM, for the full-field deformation reconstruction of solid or thin-walled beams. Shape reconstruction is performed by matching a set of analytical and experimental beam sectional strains in a least-squares sense. The main advantage of the methodology is that it can be used to monitor prismatic beams with any general cross-sectional profile. Compared to conventional approaches, accurate reconstruction can be achieved without a system model and using only a very sparse set of strain measurements. Experimental studies applying the 1D iFEM on a thin-walled C beam and an additively manufactured airfoil beam using various low- and high-order inverse beam elements were presented. Results revealed iTM2D0, iTM2D1, and iTM2D0^w elements to be accurate, with iTM2D0 providing the best compromise between reconstruction accuracy and the number of sensors required. Also, the studies demonstrated the capability of the 1D iFEM for monitoring additively manufactured beam structures. In the results presented, despite the presence of damage on the beam leading to an imperfect clamp condition, a displacement filtering technique was proposed to accurately compare the elastic deformation of the beam with iFEM predictions.

Despite the achievements of the present work in analysing the damaged beam, additional work is required for the iFEM shape sensing of similar structures with non-trivial boundary conditions. The use of an inverse shell model of the structure with problem-specific boundary conditions is an appealing solution to the problem, and further developments on this topic would be interesting to the shape sensing research community. Future work also aims to apply the proposed methodology for beams undergoing large deformations and to investigate the effect of the cross-sectional location of sensors on reconstruction accuracy.

Acknowledgements

The authors acknowledge the contributions of Dr. Massimiliano Mattone and of Dr. Marco Esposito during the experimental activity.

Appendix A

The shape functions are defined in the natural coordinates, $\eta = \frac{2x}{l_e} - 1$, where l_e is the element length ($\eta \in [-1, 1]$).
Lagrange polynomial of degree-1,

$$L_1^{(1)} = \frac{1}{2}(1-\eta) \quad , \quad L_2^{(1)} = \frac{1}{2}(1+\eta) \tag{A.1}$$

Lagrange polynomial of degree-2,

$$L_1^{(2)} = \frac{1}{2}\eta(\eta-1) \quad , \quad L_r^{(2)} = (1-\eta^2) \quad , \quad L_2^{(2)} = \frac{1}{2}\eta(\eta+1) \tag{A.2}$$

Lagrange polynomial of degree-4,

$$\begin{aligned} L_1^{(4)} =& \frac{1}{6}\eta(4\eta^2-1)(\eta-1) \quad , \quad L_q^{(4)} = \frac{4}{3}\eta(1-\eta^2)(2\eta-1) \\ L_r^{(4)} =& (1-\eta^2)(1-4\eta^2) \quad , \\ L_s^{(4)} =& \frac{4}{3}\eta(1-\eta^2)(2\eta+1) \quad , \quad L_2^{(4)} = \frac{1}{6}\eta(4\eta^2-1)(\eta+1) \end{aligned} \tag{A.3}$$

Cubic functions derived for iTM2D0 [21],

$$\begin{aligned} N_1^{(3)} =& \frac{l_e}{24}(1-\eta^2)(2\eta-3) \quad , \quad N_r^{(3)} = -\frac{l_e}{6}\eta(1-\eta^2) \\ N_2^{(3)} =& \frac{l_e}{24}(1-\eta^2)(2\eta+3) \end{aligned} \tag{A.4}$$

Cubic functions derived for iTM2D1 [21],

$$
\begin{aligned}
M_1^{(3)} =& \frac{4}{3l_e}(1-\eta^2)(4\eta-3) \quad , \quad M_q^{(3)} = -\frac{8}{3l_e}(1-\eta^2)(8\eta-3) \\
M_r^{(3)} =& \frac{32}{l_e}(1-\eta^2)\eta \quad , \\
M_s^{(3)} =& -\frac{8}{3l_e}(1-\eta^2)(8\eta+3) \quad , \quad M_2^{(3)} = \frac{4}{3l_e}(1-\eta^2)(4\eta+3)
\end{aligned}
\tag{A.5}
$$

Appendix B

Based on the kinematic assumptions of classical beam theory, the Cartesian components of the displacement vector can be defined in terms of the kinematic variables $\mathbf{u} \equiv \{u, v, w\}^T$ as [24]

$$
\begin{aligned}
u_x(x,y,z) &= u(x) + zw_{,x}(x) - yv_{,x}(x) \\
u_y(x,y,z) &= v(x) \\
u_z(x,y,z) &= w(x)
\end{aligned}
\tag{B.1}
$$

Substituting Eq. B.1 in the linear strain-displacement relations, the non-zero components of the strain vector yield the analytical sectional strains e_i $(i = 1, ..., 3)$ of the element

$$
\mathbf{e}(\mathbf{u}) = \{e_1, e_2, e_3\}^T = \{u_{,x}, w_{,xx}, -v_{,xx}\}^T \tag{B.2}
$$

The kinematic variables are interpolated within the element as follows

$$
\begin{aligned}
u(x) =& L_1(x)u_1 + L_2(x)u_2 \\
v(x) =& H_1(x)v_1 + H_2(x)\theta_1 + H_3(x)v_2 + H_4(x)\theta_2 \\
w(x) =& H_1(x)w_1 + H_2(x)\phi_1 + H_3(x)w_2 + H_4(x)\phi_2
\end{aligned}
\tag{B.3}
$$

where $x \in [0, l_e]$ and the Lagrange polynomials L_i $(i = 1, 2)$ and the Hermitian polynomials H_i $(i = 1, ..., 4)$ are

$$
\begin{aligned}
L_1(x) =& 1 - \frac{x}{l_e} \qquad , \qquad L_2(x) = \frac{x}{l_e} \\
H_1(x) =& 1 - \frac{3x^2}{l_e^2} + \frac{2x^3}{l_e^3} \qquad , \qquad H_2(x) = x - \frac{2x^2}{l_e} + \frac{x^3}{l_e^2} \\
H_3(x) =& \frac{3x^2}{l_e^2} - \frac{2x^3}{l_e^3} \qquad , \qquad H_4(x) = -\frac{x^2}{l_e} + \frac{x^3}{l_e^2}
\end{aligned}
\tag{B.4}
$$

As the axial strain, e_1, is a constant, and the curvatures, e_2 and e_3, are interpolated linearly, accurate integration requires sectional strains from at least two axial sections of the element (at least 6 strain measurements).

Appendix C

The shear coefficients for the thin-walled C beam (see Fig. C.1) are computed using numerical strain data from a high-fidelity FEM model developed in ABAQUS and modelled with 355520 8-node linear brick elements (C3D8R). The values calculated are reported in Table. C.1, where k_{ty} and k_{tz} are the shear correction factors of the profile (defined in Ref. [37]).

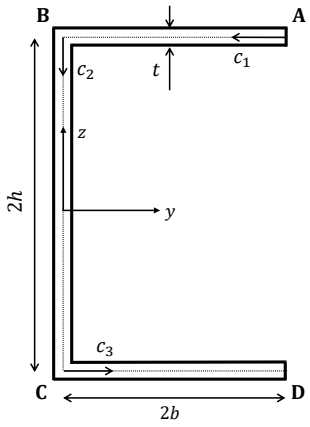

Figure C.1: Dimensions and midline coordinates of the thin-walled section

The tangential shear variation γ_{xc} [37] due to unit transverse loads along the z and $y-$axis are estimated using the Jourawski formula [45] and defined in Table C.2. The shear functions f_1 and f_2 can be estimated from these quantities

Table C.1: Dimensions and shear coefficients for the thin-walled C section

$2h$	$2b$	t	k_{ty}	$k_{\epsilon y}$	k_{tz}	$k_{\epsilon z}$
43 mm	29 mm	2 mm	0.4077	1.0589	0.3355	1.1580

by normalizing with respect to the maximum value. The second area moments, I_{yy} and I_{zz}, are calculated at the section centroid, $(y_c, z_c) = (\frac{2b^2}{2b+h}, 0)$ (defined based on Fig. C.1). The torsional functions, f_3 and f_3^w, are computed using the same high-fidelity FEM model. A constant value of $f_3 \approx f_3^w = 0.00285$ is estimated over the outer sections of each flange.

Table C.2: Functions for the thin-walled section along the flange mid-line

Function	Section flange		
	AB	BC	CD
$-\gamma_{xc}^z \times (I_{yy}t)$	thc_1	$2bth + tc_2(h - \frac{c_2}{2})$	$2bth - thc_3$
$-\gamma_{xc}^y \times (I_{zz}t)$	$tc_1(2b - \frac{c_1}{2} - y_c)$	$2bt(b - y_c) - tc_2 y_c$	$2bt(b - y_c) - 2hty_c$ $+tc_3(\frac{c_3}{2} - y_c)$

The shear coefficients and functions for the thin-walled airfoil beam (analysed in Section 4) are computed numerically using strain data from a high-fidelity FEM model developed in ABAQUS (modelled with 492382 C3D8R elements). These quantities are reported in Table C.3 where c is the circumferential coordinate defined from the trailing to the leading edge and p is the perimeter of the airfoil.

Table C.3: Dimensions and shear coefficients for the thin-walled airfoil beam

k_{ty}	$k_{\epsilon y}$	k_{tz}	$k_{\epsilon z}$	f_1	f_2	f_3
0.854	0.799	0.042	2.952	$\sin\left(\frac{3\pi c}{2p}\right)$	$-\sin\left(\frac{\pi c}{p}\right)$	0.01

References

[1] C. R. Farrar and K. Worden. An Introduction to Structural Health Monitoring. *Philosophical Transactions of the Royal Society A: Mathemati-*

cal, Physical and Engineering Sciences, 365(1851):303–315, 2007. ISSN 1364503X. doi: 10.1098/rsta.2006.1928.

[2] J. Valasek. *Morphing Aerospace Vehicles and Structures*. John Wiley & Sons, 2012.

[3] T. A. Weisshaar. Morphing aircraft systems: Historical perspectives and future challenges. *Journal of Aircraft*, 50(2):337–353, 2013. ISSN 15333868. doi: 10.2514/1.C031456.

[4] M. Gherlone, P. Cerracchio, and M. Mattone. Shape sensing methods: Review and experimental comparison on a wing-shaped plate. *Progress in Aerospace Sciences*, 99:14–26, April, 2018. ISSN 03760421. doi: 10.1016/j.paerosci.2018.04.001.

[5] W. L. Ko, W. L. Richards, and V. T. Tran. Displacement Theories for In-Flight Deformed Shape Predictions of Aerospace Structures. *NASA/TP-2007-214612*, 2007.

[6] H. Xu, Q. Zhou, L. Yang, M. Liu, D. Gao, Z. Wu, and M. Cao. Reconstruction of full-field complex deformed shapes of thin-walled special-section beam structures based on in situ strain measurement. *Advances in Structural Engineering*, 23(15):3335–3350, 2020. ISSN 20484011. doi: 10.1177/1369433220937156.

[7] L. H. Kang, D. K. Kim, and J. H. Han. Estimation of dynamic structural displacements using fiber Bragg grating strain sensors. *Journal of Sound and Vibration*, 305(3):534–542, 2007. ISSN 10958568. doi: 10.1016/j.jsv.2007.04.037.

[8] M. A. Davis, A. D. Kersey, J. Sirkis, and E. J. Friebele. Shape and vibration mode sensing using a fiber optic Bragg grating array. *Smart Materials and Structures*, 5(6):759–765, 1996. ISSN 09641726. doi: 10.1088/0964-1726/5/6/005.

[9] R. Bruno, N. Toomarian, and M. Salama. Shape estimation from incomplete measurements: A neural-net approach. *Smart Materials and Structures*, 3(2):92–97, 1994. ISSN 09641726. doi: 10.1088/0964-1726/3/2/002.

[10] A. Tessler and J. L. Spangler. A Variational Principle for Reconstruction of Elastic Deformations in Shear Deformable Plates and Shells. *NASA/TM-2003-212445*, 2003.

[11] A. Tessler and J. L. Spangler. A least-squares variational method for full-field reconstruction of elastic deformations in shear-deformable plates and shells. *Computer Methods in Applied Mechanics and Engineering*, 194(2-5 SPEC. ISS.):327–339, 2005. ISSN 00457825. doi: 10.1016/j.cma.2004.03.015.

[12] A. Tessler and J. Spangler. Inverse FEM for Full-Field Reconstruction of Elastic Deformations in Shear Deformable Plates and Shells. *Proceedings of Second European Workshop on Structural Health Monitoring*, pages 83–90, 2004.

[13] A. Kefal, E. Oterkus, A. Tessler, and J. L. Spangler. A quadrilateral inverse-shell element with drilling degrees of freedom for shape sensing and structural health monitoring. *Engineering Science and Technology, an International Journal*, 19(3):1299–1313, 2016. ISSN 22150986. doi: 10.1016/j.jestch.2016.03.006. URL `http://dx.doi.org/10.1016/j.jestch.2016.03.006`.

[14] A. Kefal. An efficient curved inverse-shell element for shape sensing and structural health monitoring of cylindrical marine structures. *Ocean Engineering*, 188:106262, 2019. ISSN 00298018. doi: 10.1016/j.oceaneng.2019.106262. URL `https://doi.org/10.1016/j.oceaneng.2019.106262`.

[15] A. Kefal, A. Tessler, and E. Oterkus. An enhanced inverse finite element method for displacement and stress monitoring of multilayered

composite and sandwich structures. *Composite Structures*, 179:514–540, 2017. doi: https://doi.org/10.1016/j.compstruct.2017.07.078. URL https://doi.org/10.1016/j.compstruct.2017.07.078.

[16] M. Li, D. Jia, Z. Wu, S. Qiu, and W. He. Structural damage identification using strain mode differences by the ifem based on the convolutional neural network (cnn). *Mechanical Systems and Signal Processing*, 165:108289, 2022. ISSN 0888-3270. doi: https://doi.org/10.1016/j.ymssp.2021.108289.

[17] A. Kefal, C. Diyaroglu, M. Yildiz, and E. Oterkus. Coupling of peridynamics and inverse finite element method for shape sensing and crack propagation monitoring of plate structures. *Computer Methods in Applied Mechanics and Engineering*, 391:114520, 2022. ISSN 0045-7825. doi: https://doi.org/10.1016/j.cma.2021.114520.

[18] F. Ganjdoust, A. Kefal, and A. Tessler. A novel delamination damage detection strategy based on inverse finite element method for structural health monitoring of composite structures. *Mechanical Systems and Signal Processing*, 192:110202, 2023. ISSN 0888-3270. doi: https://doi.org/10.1016/j.ymssp.2023.110202.

[19] R. Roy and M. Gherlone. Delamination and skin-spar debond detection in composite structures using the inverse finite element method. *Materials*, 16(5), 2023. ISSN 1996-1944. doi: 10.3390/ma16051969. URL https://www.mdpi.com/1996-1944/16/5/1969.

[20] L. Colombo, D. Oboe, C. Sbarufatti, F. Cadini, S. Russo, and M. Giglio. Shape sensing and damage identification with ifem on a composite structure subjected to impact damage and non-trivial boundary conditions. *Mechanical Systems and Signal Processing*, 148:107163, 2021. ISSN 0888-3270. doi: https://doi.org/10.1016/j.ymssp.2020.107163.

[21] M. Gherlone, P. Cerracchio, M. Mattone, M. Di Sciuva, and A. Tessler. Shape sensing of 3D frame structures using an inverse Finite Element

Method. *International Journal of Solids and Structures*, 49(22):3100–3112, 2012. ISSN 00207683. doi: 10.1016/j.ijsolstr.2012.06.009.

[22] S. Timoshenko. *Strength of Materials*. Van Nostrand Company Inc, Princeton, USA, 1956.

[23] M. Gherlone, P. Cerracchio, M. Mattone, M. Di Sciuva, and A. Tessler. An inverse finite element method for beam shape sensing: theoretical framework and experimental validation. *Smart Mater. Struct.*, pages 578–585, 2014. doi: http://dx.doi.org/10.1088/0964-1726/23/4/045027.

[24] P. Savino, M. Gherlone, and F. Tondolo. Shape sensing with inverse finite element method for slender structures. *Structural Engineering and Mechanics*, 72(2):77–87, 2019. doi: https://dx.doi.org/10.12989/sem.2019.72.2.217.

[25] F. Zhao, H. Bao, J. Liu, and K. Li. Shape sensing of multilayered composite and sandwich beams based on Refined Zigzag Theory and inverse finite element method. *Composite Structures*, 261:113321, 2021. ISSN 02638223. doi: 10.1016/j.compstruct.2020.113321.

[26] P. Savino, F. Tondolo, M. Gherlone, and A. Tessler. Application of inverse finite element method to shape sensing of curved beams. *Sensors (Switzerland)*, 20(24):1–16, 2020. ISSN 14248220. doi: 10.3390/s20247012.

[27] P. Savino, M. Gherlone, F. Tondolo, and R. Greco. Shape-sensing of beam elements undergoing material nonlinearities. *Sensors (Switzerland)*, 21(2): 1–17, 2021. ISSN 14248220. doi: 10.3390/s21020528.

[28] F. Zhao, L. Xu, H. Bao, and J. Du. Shape sensing of variable cross-section beam using the inverse finite element method and isogeometric analysis. *Measurement: Journal of the International Measurement Confederation*, 158:107656, 2020. ISSN 02632241. doi: 10.1016/j.measurement.2020.107656.

[29] F. Zhao and H. Bao. An improved inverse finite element method for shape sensing using isogeometric analysis. *Measurement*, 167:108282, 2021. ISSN 0263-2241. doi: https://doi.org/10.1016/j.measurement.2020.108282.

[30] K. Chen, K. Cao, G. Gao, and H. Bao. Shape sensing of Timoshenko beam subjected to complex multi-node loads using isogeometric analysis. *Measurement: Journal of the International Measurement Confederation*, 184: 109958, 2021. ISSN 02632241. doi: 10.1016/j.measurement.2021.109958.

[31] R. You and L. Ren. An enhanced inverse beam element for shape estimation of beam-like structures. *Measurement: Journal of the International Measurement Confederation*, 181:109575, 2021. ISSN 02632241. doi: 10.1016/j.measurement.2021.109575.

[32] Y. Zhao, J. Du, H. Bao, and Q. Xu. Optimal Sensor Placement for Inverse Finite Element Reconstruction of Three-Dimensional Frame Deformation. *International Journal of Aerospace Engineering*, 18, 2018. ISSN 16875974. doi: 10.1155/2018/6121293.

[33] Y. Zhao, J. Du, H. Bao, and Q. Xu. Optimal sensor placement based on eigenvalues analysis for sensing deformation of wing frame using iFEM. *Sensors (Switzerland)*, 18(8), 2018. ISSN 14248220. doi: 10.3390/s18082424.

[34] Xiaohan Li, Shengtao Niu, Hong Bao, and Naigang Hu. Improved adaptive multi-objective particle swarm optimization of sensor layout for shape sensing with inverse finite element method. *Sensors*, 22(14), 2022. ISSN 1424-8220. doi: 10.3390/s22145203.

[35] Y. Zhao, J. Du, Q. Xu, and H. Bao. Real-time monitoring of the position and orientation of a radio telescope sub-reflector with fiber bragg grating sensors. *Sensors (Switzerland)*, 19(3), 2019. ISSN 14248220. doi: 10.3390/s19030619.

[36] R. Roy, M. Gherlone, and C. Surace. Shape sensing of beams with complex cross sections using the inverse finite element method. *In Proceeding of 12th International Workshop on Structural Health Monitoring, Stanford, CA*, 2019.

[37] R. Roy, M. Gherlone, and C. Surace. A shape sensing methodology for beams with generic cross-sections: Application to airfoil beams. *Aer. Sci. and Tech.*, 110:106484, 2021. ISSN 1270-9638.

[38] R. Roy. *Developing Advanced Shape Sensing Methodologies for Aerospace Applications*. Doctoral dissertation, Politecnico di Torino, 2022.

[39] V. Z. Vlasov. *Thin-Walled Elastic Beams*. Fizmatgiz, Moscow, 1959.

[40] S. P. Timoshenko. Theory of bending, torsion and buckling of thin-walled members of open cross section. *Journal of the Franklin Institute*, 239 (3):201–219, 1945. ISSN 0016-0032. doi: https://doi.org/10.1016/0016-0032(45)90093-7.

[41] H.W. Engl, M. Hanke, and A. Neubauer. *Regularization of Inverse Problems, in: Mathematics and its Applications*. Kluwer Academic Publishers, Dordrecht, 1996.

[42] A. Tessler, R. Roy, M. Esposito, C. Surace, and M. Gherlone. Shape Sensing of Plate and Shell Structures Undergoing Large Displacements Using the Inverse Finite Element Method. *Shock and Vibration*, 2018, 2018. ISSN 10709622. doi: 10.1155/2018/8076085.

[43] A. Kefal, I. E. Tabrizi, M. Yildiz, and A. Tessler. A smoothed ifem approach for efficient shape-sensing applications: Numerical and experimental validation on composite structures. *Mechanical Systems and Signal Processing*, 152:107486, 2021. ISSN 0888-3270. doi: https://doi.org/10.1016/j.ymssp.2020.107486.

[44] D. Oboe, C. Sbarufatti, and M. Giglio. Physics-based strain pre-extrapolation technique for inverse finite element method. *Mechanical Systems and Signal Processing*, 177:109167, 2022. ISSN 0888-3270. doi: https://doi.org/10.1016/j.ymssp.2022.109167.

[45] A. Carpinteri. *Structural Mechanics Fundamentals*. CRC Press, FL, USA, 2013.